UNIVERSITÀ degli STUDI di LECCE
Dipartimento di Fisica
Dottorato di Ricerca in Fisica – XVIII Ciclo

Track finding for positrons in the MEG experiment

Ph.D. Student:
Claudio CHIRI

Advisor:
Dr. **Stefania SPAGNOLO**

July 2006

Contents

Introduction

After the neutrino oscillation phenomena were observed a renewed considerable interest in Lepton Flavor Violation has arisen. This is due to the fact that in many alternative theories to the Minimal Standard Model, introduced in order to obtain a possible answer to its open questions, LFV processes are predicted with sizable branching ratios. Thus, there are many theoretical scenarios which accommodate branching ratios for LFV processes at a level accessible in future experiments. Therefore, LFV searches have robust potential to discover new physics beyond the SM.

One of the most promising channel is the $\mu^+ \to e^+\gamma$ decay which is also appealing from an experimental point of view, due to the big progress and in the technology producing high–intensity muon beams.

In this work, after a brief review of the Standard Model, of its possible extensions which give origin to lepton flavor violation (chapter 1), the predictions for a typical LFV process, as the $\mu^+ \to e^+\gamma$ decay, are discussed (chapter 2).

A new experiment, called MEG and described in chapter 3, is under development at the Paul Scherrer Institute (PSI) of Zurich (CH). It aims to achieve a sensitivity of 5×10^{-14} on the $\mu^+ \to e^+\gamma$ branching ratio, improving the constrains on such process by two orders of magnitudes with respect to the present limit, 1.2×10^{-11} with 90% C.L., in case of no signal detection.

This performance depends on the detector intrinsic efficiency and resolution, but also on the efficiencies of the event reconstruction algorithms.

The main subject of this work is the development of a strategy to perform the reconstruction of the positron tracks in the MEG Spectrometer. In particular, in chapter 4 a software framework, MegRoot, designed for the whole data processing and analysis of the MEG experiment will be described.

Chapters 5 and 6 are devoted to the discussion of the algorithms for track

finding and track fitting in the Spectrometer. Results from the analysis of samples of simulated events are also presented.

Chapter 1

Lepton Flavor Violation and the physics beyond the Standard Model

The search for Lepton Flavor Violating phenomena (LFV) represents an important way to discover new physics beyond the Standard Model (SM). As matter of fact, while in the minimal SM, with only one Higgs doublet and vanishing neutrino masses, lepton flavor is conserved as direct consequence of gauge invariance and of the renormalization of the SM Lagrangian, in many scenarios of physics beyond the SM, LFV could occur from various sources. In particular, Super-symmetric (SUSY) extensions of the SM and Super-symmetric Grand Unified Theories (SUSY–GUT) often imply sizable LFV effects.

Recently, the evidence for neutrino oscillations, based on the Solar neutrino deficit and the atmospheric neutrino anomaly[1], has driven a considerable growth of interest for the theoretical aspects of LFV and their phenomenological implications.

In the following, we will discuss how the detection and the investigations of LFV processes would provide an opportunity to probe physics at a very high energy scales, like either the GUT scale or the mass scale of a heavy right–handed Majorana neutrino for the see–saw mechanism.

In this chapter, after a summary of the SM, we intend to illustrate the theoretical models that foresee LFV effects and, hereafter, the possible mechanisms responsible for neutrino oscillations.

1.1 The Standard Model

All known particle physics phenomena are extremely well described within the Standard Model of elementary particles and their fundamental interactions. The SM provides a very elegant theoretical framework and it has successfully passed very precise experimental tests in the past decades.

1.1.1 The Standard Model Lagrangian

The SM[2] is a gauge theory[3] based on the gauge symmetry group $SU(3)_C \times SU(2)_L \times U(1)_Y$, which encloses itself two different theories:

- the Quantum Cromo–Dynamics (QCD), describing the strong interactions between quarks and gluons[4];
- the Glashow–Salam–Weinberg theory for the electroweak interactions [5].

The strong interactions are described by the Lagrangian:

$$\mathcal{L}_{SU(3)_C} = \sum_r \overline{q}_{r\alpha} i \not{D}^{\alpha}_{\beta} q^{\beta}_r - \frac{1}{4} F^i_{\mu\nu} F^{i\ \mu\nu} \tag{1.1}$$

The first term describes the strong interactions among the quarks. Quarks manifest, themselves, in three color species, as indicated by the α and β indexes, and in three flavors (r is the family index). The gluons fields G^i_μ ($i = 1, ...8$) couple to quarks of different color but same family, according to the structure of the covariant derivative

$$D^{\alpha}_{\mu\beta} = \partial_\mu \delta^{\alpha}_{\beta} + i g_s G^i_\mu \frac{\lambda^{i\alpha}_{\beta}}{2} \tag{1.2}$$

where g_s is the strong coupling constant and λ^is are the Gell–Mann matrices generators of the $SU(3)_C$ group. In (1.1) there are not mass terms for the quarks, because they will be generated later by spontaneous symmetry breaking.

The second term in (1.1) contains the strength tensor for gluons defined as follows

$$F^i_{\mu\nu} = \partial_\mu G^i_\nu - \partial_\nu G^i_\mu - g_s f_{ijk} G^j_\mu G^k_\nu \tag{1.3}$$

where f_{ijk} are the structure constants of $SU(3)_C$ defining the commutation relation of the λ matrices

$$[\lambda^i, \lambda^j] = 2 i f_{ijk} \lambda^k$$

The gauge structure of $SU(3)_C$ implies that three and four point self–interactions among gluons are allowed as evident from (1.1). As already mentioned, the color interactions among quarks are diagonal in the flavor indexes but change the quark colors.

The electroweak theory is based on the $SU(2)_L \times U(1)_Y$ Lagrangian

$$\mathcal{L}_{SU(2)_L \times U(1)_Y} = \mathcal{L}_{gauge} + \mathcal{L}_{\phi} + \mathcal{L}_{fermions} + \mathcal{L}_{Yukawa} \tag{1.4}$$

The gauge part is

$$\mathcal{L}_{gauge} = -\frac{1}{4} F^i_{\mu\nu} F^{i\ \mu\nu} - \frac{1}{4} B_{\mu\nu} B^{\mu\nu} \tag{1.5}$$

where

$$\begin{aligned} B_{\mu\nu} &= \partial_\mu B_\nu - \partial_\nu B_\mu \\ F^i_{\mu\nu} &= \partial_\mu W^i_\nu - \partial_\nu B^i_\mu - g\epsilon_{ijk} W^j_\mu W^k_\nu \end{aligned}$$

are the field strength tensors for W^i_μ $(i = 1, 2, 3)$ and B_μ $SU(2)_L$ and $U(1)_Y$ gauge fields, g is the gauge coupling constant of $SU(2)$ and ϵ_{ijk} is the totally antisymmetric tensor.

The third component of weak isospin (T_3) and hypercharge (Y) are related to the electric charge operator by the relation

$$Q = T_3 + \frac{Y}{2}$$

The scalar sector of the Lagrangian has the form

$$\mathcal{L}_{\varphi} = (D^\mu \varphi)^\dagger D_\mu \varphi - V(\varphi) \tag{1.6}$$

where $\varphi = \begin{pmatrix} \varphi^+ \\ \varphi^0 \end{pmatrix}$ is a complex scalar field, which is a doublet under $SU(2)$ with hypercharge $Y_\varphi = +\frac{1}{2}$, and $V(\varphi)$ is the Higgs potential.

The covariant derivative is defined, for $SU(2)_L$ doublets like

$$D_\mu = \left(\partial_\mu + ig\frac{\tau_i}{2} W^i_\mu + ig'\frac{Y}{2} B_\mu \right)$$

where τ_i are the Pauli matrices and g' is the gauge coupling constant of the $U(1)$ group related to g by the weak angle $(\theta_W = \tan^{-1}(g'/g))$, while for $SU(2)_L$ singlets it is given by

$$D_\mu = \left(\partial_\mu + ig'\frac{Y}{2} B_\mu \right)$$

The combination of $SU(2)_L \times U(1)_Y$ invariance and renormalization restricts V to the form

$$V(\varphi) = \mu^2 \varphi^\dagger \varphi + \lambda \left(\varphi^\dagger \varphi\right)^2 \tag{1.7}$$

in particular the vacuum stability requires $\lambda > 0$, while a $\mu^2 < 0$ is needed for spontaneous symmetry breaking.

The fermion term is

$$\begin{aligned} \mathcal{L}_{fermion} &= \sum_{m=1}^{3} (\overline{q}_{mL} i \not{D} q_{mL} + \overline{l}_{mL} i \not{D} l_{mL} + \overline{u}_{mR} i \not{D} u_{mR} + \\ &\quad \overline{d}_{mR} i \not{D} d_{mR} + \overline{e}_{mR} i \not{D} e_{mR}) \end{aligned} \tag{1.8}$$

where m is the family index and $L(R)$ refer to the left(right) chiral projections of a Dirac spinor

$$\psi_{L,R} = \frac{1 \mp \gamma_5}{2} \psi \tag{1.9}$$

Left–handed quarks and leptons

$$q_{mL} = \begin{pmatrix} u_m \\ d_m \end{pmatrix}_L \qquad l_{mL} = \begin{pmatrix} \nu_m \\ e_m^- \end{pmatrix}_L$$

transform as $SU(2)_L$ doublets and have hypercharge $\frac{1}{6}$ and $-\frac{1}{2}$ respectively, while the right–handed fields

$$u_{mR},\ d_{mR},\ e_{mR}^-$$

are singlets under weak isospin and have hypercharge equal to their electric charge.

The last term in (1.4) is

$$-\mathcal{L}_{Yukawa} = \sum_{m,n=1}^{F} \left[\bar{q}_{mL} \lambda^u_{mn} \tilde{\varphi} u_{nR} + \bar{q}_{mL} \lambda^d_{mn} \varphi d_{nR} + \bar{l}_{mL} \lambda^e_{mn} \varphi e_{nR}\right] + h.c. \tag{1.10}$$

where the matrices λ_{mn} describe the Yukawa couplings between the Higgs doublet φ[1] and the various flavors m and n of quarks and leptons.

1.1.2 Spontaneous Symmetry Breaking

Gauge invariance and renormalization do not allow mass terms in the Lagrangian for the gauge bosons or for chiral fermions. On the other hand,

[1] $\tilde{\varphi}$ is defined as $i\tau_2 \varphi^\dagger$

massless gauge bosons are not acceptable for the weak interactions which are known to be short–ranged. The only way to produce effective masses, for bosons and matter particles, is to assume that the vacuum (i.e. the lowest energy state) do not respect the Lagrangian symmetry.

If we rewrite the Higgs doublet in terms of four real fields

$$\varphi = \begin{pmatrix} \varphi^+ \\ \varphi^0 \end{pmatrix} = \begin{pmatrix} \frac{1}{\sqrt{2}}(\varphi_1 - i\varphi_2) \\ \frac{1}{\sqrt{2}}(\varphi_3 - i\varphi_4) \end{pmatrix} \tag{1.11}$$

the potential (1.7) becomes

$$V(\varphi) = \frac{1}{2}\mu^2 \sum_{i=1}^{4} {\varphi_i}^2 + \frac{1}{4}\lambda \left(\sum_{i=1}^{4} {\varphi_i}^2 \right)^2 \tag{1.12}$$

which has its minimum at $|\varphi| = \sqrt{-\frac{\mu^2}{2\lambda}}$.
This manifold of points that are minimizing $V(\varphi)$ are invariant under $SU(2)$ transformations. Any choice of a particular value of φ (φ_0) breaks the symmetry and generate a mass term in the Lagrangian for the corresponding gauge boson. However, if the vacuum φ_0 is still left invariant by some subgroup of gauge transformations, then the gauge boson associated with this subgroup will remain massless.

The appropriate choice to generate the observed boson masses is

$$< 0|\varphi_i|0 >= 0 \qquad \text{for } i = 1, 2, 4 \qquad \text{and} \qquad < 0|\varphi_3|0 >= v$$

this vacuum value is not invariant under T_1, T_2 and $T_3 - \frac{Y}{2}$, but it is invariant under $T_3 + \frac{Y}{2}$. As a consequence by expanding the fourth field around this vacuum value, the equation (1.6) gives masses (M_W and M_Z) for the $W^\pm$ and the Z fields defined as follows

$$W^\pm = \frac{1}{\sqrt{2}}\left(W^1 \mp iW^2\right)$$

$$Z = -\sin\theta_W B + \cos\theta_W W^3$$

$$M_W = \frac{vg}{2} \qquad M_Z = \sqrt{g^2 + {g'}^2}\frac{v}{2}$$

while the photon field

$$A \;=\; \cos\theta_W B + \sin\theta_W W^3$$

remains massless.

Analogously, the same mechanism gives masses to the leptons and quarks. For example, to generate the electron mass, we can consider the expansion of the φ field around the vacuum $\varphi = \begin{pmatrix} \varphi^+ \\ \varphi^0 \end{pmatrix} = \frac{1}{\sqrt{2}} \begin{pmatrix} 0 \\ v + h(x) \end{pmatrix}$. in (1.10), which becomes, at first order,

$$-\mathcal{L} = \frac{\lambda_e}{\sqrt{2}} v \left(\bar{e}_L e_R + \bar{e}_R e_L \right) \tag{1.13}$$

We now choose λ_e so that

$$m_e = \frac{\lambda_e v}{\sqrt{2}} \tag{1.14}$$

and taking in account that

$$m_e \bar{e} e = m_e \bar{e} \left[\frac{1}{2} \left(1 - \gamma^5 \right) + \frac{1}{2} \left(1 + \gamma^5 \right) \right] e = m_e \left(\bar{e}_R e_L + \bar{e}_L e_R \right) \tag{1.15}$$

we obtain the required electron mass

$$-\mathcal{L} = m_e \bar{e} e \tag{1.16}$$

Note however that, since λ_e is arbitrary, the actual mass of the electron is not predict.
The quark masses are generated in the same way.

1.1.3 Motivations for new physics

As we have discussed, the Standard Model is a mathematically consistent renormalizable field theory, which predicts or is consistent with all experimental facts. However, there are several reasons why it is widely believed that it does not give the full picture of nature. The shortcomings of the SM are, usually, summarized as a number of problems:

1. Gauge Problems
The SM is a complicated direct product of three subgroups with separate gauge couplings; there is not explanation for why only the electroweak part is chiral (parity violating); similarly, it does not explain the charge quantization, i.e., why all particles have charges which are multiples of $e/3$.

2. Fermion Problem
The SM gives no explanation for the existence for several families and no prediction for their number. Furthermore, there is no explanation or prediction

Ordinary particles		SUSY particles	
Particle	Spin	Particle	Spin
quark (q)	$\frac{1}{2}$	squark ($\tilde{q}$)	0
lepton (l)	$\frac{1}{2}$	slepton ($\tilde{l}$)	0
gluon (G)	1	gluino ($\tilde{G}$)	$\frac{1}{2}$
$W^{\pm}$, Z^0, γ	1	chargino ($\tilde{\chi}_i^{\pm}$ $i = 1, 2$)	$\frac{1}{2}$
Higgs boson (h, H, A, $H^{\pm}$)	0	neutralino ($\tilde{\chi}_i^0$ $i = 1, 2, 3, 4$)	$\frac{1}{2}$

Table 1.1: *Particle Contents in the MSSM*

of the fermions masses, which vary over at least five orders of magnitude, or of the CKM mixing.

3. Higgs/hierarchy Problem
In the SM one introduces an elementary Higgs field into the theory to generate masses for the W, Z, and fermions. For the model to be consistent the Higgs mass should not be too different from the W mass. If M_H is larger than M_W by many orders of magnitude there would be a hierarchy problem, and the Higgs self–interactions would be excessively strong.

Possible answers for this problems are usually found in the alternative theories, like SuperSymmetric Models, Grand Unified Theory, Extra–Dimensions and String Theories, which embed the SM as low–energy limit.

1.2 Supersymmetric Models

Phenomenological applications of SUSY theories have been considered since the late 1970 in connection with the hierarchy problem in the SM. If the SM is regarded as a low–energy approximation of a more complete theory, which sets in at high energy scale (close to the Planck scale 10^{19} GeV), the cancellation of the divergent contributions of the radiative corrections to the Higgs mass requires a fine tuning of the bare Higgs mass in order to keep the electroweak scale well below the high energy scale. SuperSymmetry provides a natural solution of such problem because the corresponding bosonic and fermionic loops are exactly canceled.

The minimal super–symmetric extension of the SM is called the Minimal SuperSymmetric Standard Model (MSSM). In it, each SM particle is

associated to a SUSY partner, with a spin different by $\hbar/2$. For quarks and leptons, complex scalar fields, squarks ($\tilde{q}$) and sleptons ($\tilde{l}$), are introduced. The superpartners of the gauge bosons are spin–1/2 gauge fermions generically indicated with the term "gauginos". In more detail, they are gluinos ($\tilde{G}$) associated to the SM gluons, wino and a bino ($\tilde{W}^{\pm}$, $\tilde{B}$) corresponding to the $SU(2)_{e.w.}$ gauge fields. As for the Higgs sector, the SUSY models contain at least two Higgs doublet fields. They are required separately to generate the mass terms for up–type quarks, and for down–type quarks and charged leptons. The superpartners of the Higgs field are spin–1/2 fermions and, after electroweak symmetry breaking, they mix with the wino and the bino to form two charged Dirac fermions, called charginos ($\tilde{\chi}_i^{\pm} \quad i = 1, 2$), and four Majorana fermions, called neutralinos ($\tilde{\chi}_i^0 \quad i = 1, 2, 3, 4$).

1.2.1 The SuperSymmetric Lagrangian

In a renormalizable supersymmetric theory, the interactions and masses of all the particles are determined just by their gauge transformation properties and by the superpotential (W). The latter is an analytic function of the supermultiplets, which contains as components all of the bosonic, fermionic and auxiliary fields e.g. $\Phi_i = (\phi_i, \psi_i, F_i)$ (this is analogous to the way in which one often describes a weak isospin doublet or color triplet by a multicomponent field), and can be written, in a generic form, as:

$$W = \frac{1}{2} M^{ij} \mathbf{\Phi}_i \mathbf{\Phi}_j + \frac{1}{6} y^{ijk} \mathbf{\Phi}_i \mathbf{\Phi}_j \mathbf{\Phi}_k \tag{1.17}$$

where M^{ij} is a symmetric mass matrix for the fermion fields, and y^{ijk} is a Yukawa coupling of scalar ϕ_k and two fermions $\psi_i \psi_j$ which must be totally symmetric under interchange of i, j, k.

Moreover, a realistic phenomenological model must contain supersymmetric breaking terms. In this way, supersymmetry is hidden at low energies in a manner exactly analogous to the electroweak symmetry in the ordinary SM.

Therefore, the MSSM Lagrangian can be thought as a sum of two relevant terms: the SUSY invariant Lagrangian term and the soft SUSY–breaking term

$$\mathcal{L}_{SUSY} = \mathcal{L}_{SUSYinv.} + \mathcal{L}_{SUSYbreak.} \tag{1.18}$$

in which the $\mathcal{L}_{SUSYinv}$ describes both the gauge interactions and the interactions implied by the superpotential. In particular, these latter are well

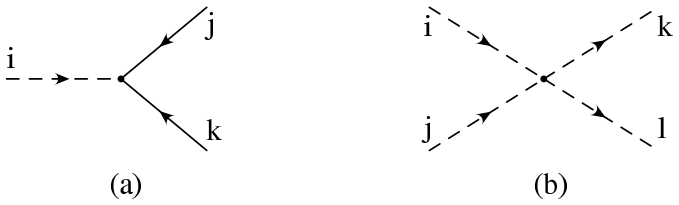

Figure 1.1: *The dimensionless non–gauge interaction vertexes in a supersymmetric theory:* a)*scalar–fermion–fermion Yukawa interaction;* b)*quartic scalar interaction.*

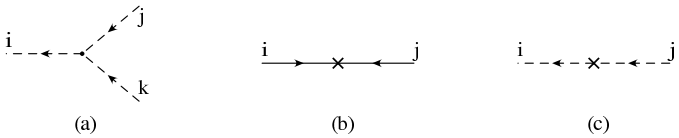

Figure 1.2: *Supersymmetric couplings:* a)*scalar interaction vertex;* b)*fermion mass term;* c)*scalar–mass term.*

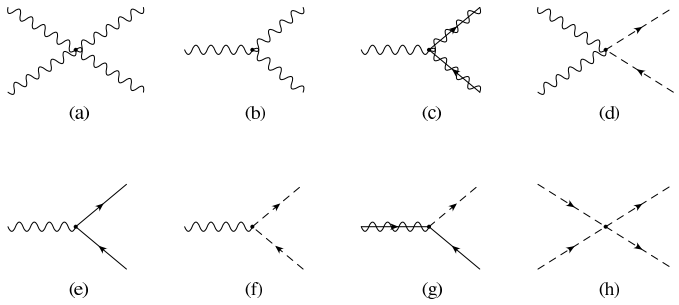

Figure 1.3: *Supersymmetric interaction vertexes. The gaugino line in the Feynman diagrams is drawn as a solid fermion line superimposed on a gauge boson squiggly line*

represented by diagrams in fig.1.1 and fig.1.2. For example, the Yukawa interaction in fig.1.1a) corresponds to terms like

$$-\frac{1}{2}y^{ijk}\phi_i\psi_j\psi_k$$

in the Lagrangian density.

In a similar way, the gauge interactions in a supersymmetric theory are shown in fig.1.3. Figures 1.3a) and 1.3b) are the interactions of gauge bosons and correspond to the term like

$$-\frac{1}{4}F_{\mu\nu}F^{\mu\nu}$$

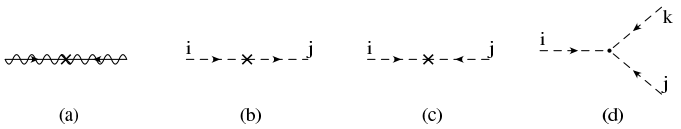

Figure 1.4: *Soft supersymmetric–breaking terms:* a) *is the Gaugino mass insertion* M_λ.

in the density Lagrangian; figure 1.3c) shows the coupling of a gaugino (the gaugino line in the Feynman diagrams is drawn as a solid fermion line superimposed on a gauge boson squiggly line) to a gauge boson; in fig.1.3g) the gaugino is coupled to a chiral fermion and a complex scalar corresponding to the term

$$-\sqrt{2}g(\phi^\star T^a \psi)\lambda^a$$

where T^a are the gauge group representation matrices, and λ^a the two–components Weyl fermion gaugino. One can think of this as the "supersymmetrization" of figures 1.3e) and 1.3f); any of these three vertexes may be obtained from any other by replacing two of the particles by their supersymmetric partners.

$\mathcal{L}_{SUSYbreak.}$ introduces interactions described by the diagrams in fig.1.4. The most relevant term is the one corresponding to the gaugino mass (fig.1.4a) and is represented in the Lagrangian density by

$$-\frac{1}{2}(M_\lambda \lambda^a \lambda^a + c.c.)$$

1.2.2 Origin of LFV

$\mathcal{L}^{SUSY}_{soft}$ introduces many new parameters which were not present in the ordinary SM. A careful count [8] reveals that there are 105 masses, phases and mixing angles in the Minimal SuperSymmetric Standard Model Lagrangian which cannot be rotated away by redefining the phases and flavor basis for the quark and lepton supermultiplets, and which have no counterpart in the ordinary SM. Most of these new parameters involve flavor mixing or CP violation processes that are forbidden in the SM. For example, if we suppose that $\mathbf{m^2_{\tilde{e}}}$, the mass matrix of the sleptons, is not diagonal in a basis ($\tilde{e}_R$,$\tilde{\mu}_R$, $\tilde{\tau}_R$) of sleptons whose super-partners are the right–handed pieces of the SM mass eigenstates e, μ, τ, slepton mixing occurs and the individual lepton numbers will not be conserved (Lepton Flavor Violation).

Similar considerations in the squark sector lead to Flavor Changing Neutral Current (FCNC) processes.

However, if the soft SUSY–breaking mass terms have a universal structure at a very high energy scale, such as the Planck scale ($\sim 10^{19}\ GeV$), the mass matrices should be diagonal with the same diagonal elements and neither FCNC nor LFV at that energy scale can be present. In the other hand, if there is some interaction which breaks lepton flavor conservation at an energy scale between the Planck and the electroweak scales, LFV could be induced in the slepton mass matrices through radiative corrections[7].

1.3 GUT Theory and LFV

Grand Unified Theory (GUT)[9][10] provides an elegant unification of the strong and electroweak forces in a larger gauge group at some high energy scale. A possible way to search signals for grand unification is to study the lepton flavor violating processes. As a matter of fact, if the GUT, characterized by a large mass scale M_G, has the pure SM as its low energy approximation, the rates for the corresponding LFV processes are unobservable; on the contrary, in a supersymmetric unified theory with supersymmetry effectively broken at the Fermi scale, $m = \mathcal{O}(G_F^{-1/2})$, the rates for the LFV low energy processes are only suppressed by powers of $1/m$[7].

The most promising GUT model are those based on the $SU(5)$ and $SO(10)$ gauge groups. In both models quarks and leptons are classified in the group supermultiplets by a spinorial representation.

The messengers of flavor violation in the lepton sector are again the soft super-symmetry breaking terms. For example, in the case of $SU(5)$, after the symmetry breaking and the scaling at low energies, the slepton mass matrices $\mathbf{m_{\tilde{e}}^2}$ can be written as

$$\mathbf{m}_{\tilde{L}}^2 = m_{\tilde{L}}^2 \mathbf{1}, \quad \mathbf{m}_{\tilde{e}_R}^2 = m_{\tilde{e}_R}^2 \mathbf{1} - \mathbf{I}_G,$$

where $\tilde{L}$ and $\tilde{e}_R$ refer to at $SU(2)$ doublet and singlet sleptons respectively, and I_G represent the lepton flavor breaking parameter depending on the model used. This determines a new not diagonal structure for the gauge couplings. If we try to diagonalize them, we must introduce two matrices $\mathbf{V}$ and $\mathbf{V}^e$: the first is the Cabibbo–Kobayashi–Maskawa matrix for the quark sector, while the second describes the mixing in the lepton sector. Under rather general assumption $\mathbf{V}^e$ elements are related to those of $\mathbf{V}$ by the

relations[12]

$$V_{ij}^{e} = yV_{ij} \quad for \quad i \neq j \quad and \quad (i \quad or \quad j) = 3, \tag{1.19}$$

$$V_{ij}^{e} = V_{ij} \quad otherwise \tag{1.20}$$

where y are the top-quark Yukawa coupling.

1.4 Neutrino Oscillations

Studies of the neutrino properties have played an essential role in the process of building our current understanding of elementary particle physics. In the SM the neutrinos have been assumed to have no electric charge, zero mass and to interact with other particles only via weak interactions. In many super symmetric extension of the SM the neutrino masses are suggested to be non–zero.

Neutrino flavor oscillation is a direct hint of small neutrino masses and it is considered today one of the most interesting phenomena in high energy physics as well as one of the most promising field to investigate in the search for new physics beyond the SM.

1.4.1 Neutrino masses

It is possible to accommodate Dirac mass terms for the neutrinos, if $SU(2)$ singlet fields describing right–handed neutrinos (ν_R) are included in the minimal SM field content. Then, mass terms of the usual form can be added to the Lagrangian, for each neutrino flavor:

$$\mathcal{L}_{Yukawa}^{\nu} = -\bar{l}_{mL}\lambda_{mn}^{\nu}\varphi^{\dagger}\nu_{nR} + h.c. \tag{1.21}$$

where λ_{mn}^{ν} is the Yukawa coupling for neutrinos. If λ_{mn}^{ν} is very small, the small masses of neutrinos can be explained.

A more natural explanation for the small neutrino masses is provided by the "see–saw mechanism"[13]. If the neutrino is a Dirac particle, it is different from its anti–particle, in analogy with the charged fermions, while if it is a Majorana particle, neutrino and anti–neutrino are just opposite chirality states of the same particle. In this case, specific mass terms can be written for R–handed neutrinos along with the Dirac mass terms; if we consider only one generation, the overall mass term in the Lagrangian is:

$$\mathcal{L}_{mass}^{\nu} = m_D\bar{\nu}_L\nu_R + M_R\bar{\nu}_R^{c}\nu_R + h.c. \tag{1.22}$$

$$= \begin{pmatrix} \bar{\nu}_L & \bar{\nu}_R^c \end{pmatrix} \begin{pmatrix} 0 & m_D \\ m_D & M_R \end{pmatrix} \begin{pmatrix} \nu_L \\ \nu_R \end{pmatrix} \tag{1.23}$$

where $\bar{\psi}^C$ is the charge conjugate field ($\bar{\psi}^C = -\psi^T C^{-1}$).

The two possible values for the neutrino physical masses are

$$m_1 \sim M_R \qquad and \qquad m_2 \sim \frac{m_D^2}{M_R}$$

Therefore, if R–handed neutrino (not yet observed at the experimentally accessible energy scale) are super–heavy (M_R very large) the other gets a tiny mass. For example if M_R is 10^{15} GeV and the Dirac mass is of the order of 100 GeV (the electroweak scale), then light neutrino masses becomes naturally $\mathcal{O}(10^{-2})$ eV.

1.4.2 Neutrino oscillations

If neutrinos are massless, the flavor eigenstates ν_e, ν_μ, ν_τ which enter in the weak interaction Lagrangian are also the mass eigenstates. However, if anyone of them has a mass, then it can happen that the mass eigenstates which we denote by ν_i ($i = 1, 2, 3$) are different from the flavor eigenstates ν_α ($\alpha = e, \mu, \tau$). In this case the flavor changing phenomena, called neutrino oscillations, can occur.

Neutrino oscillations were first discussed by Z. Maki,M. Nagakawa, S. Sakata [14] and by B. Pontecorvo [15].

The flavor states can be expressed by the superposition of the mass eigenstates as follows:

$$|\nu_\alpha\rangle = \sum_i U_{\alpha i} |\nu_i\rangle \tag{1.24}$$

where U is a unitary mixing matrix $UU^\dagger = U^\dagger U = I$. The mass eigenstates $|\nu_i\rangle$ with a finite mass m_i, momentum p and energy $E_i = \sqrt{p^2 + m_i^2}$ satisfies the following energy eigenvalue equation:

$$\mathcal{H}_0 |\nu_i\rangle = E_i |\nu_i\rangle \tag{1.25}$$

where $\mathcal{H}_0$ is the free neutrino Hamiltonian.
The time evolution of the flavor states is expressed by the Schrödinger equation

$$i\frac{d}{dt}|\nu_\alpha(t)\rangle = \mathcal{H}_0 |\nu_\alpha(t)\rangle \tag{1.26}$$

$$= \sum_i U_{\alpha i} E_i |\nu_i(t)\rangle \tag{1.27}$$

$$= \sum_{i,\beta} U_{\alpha i} E_i e^{-iE_i t} U^{\star}_{\beta i} |\nu_\beta(0)\rangle \tag{1.28}$$

The $|\nu_\alpha(t)\rangle$ can be obtained by solving this equation analytically:

$$|\nu_\alpha(t)\rangle = \sum_{i,\beta} U_{\alpha i} e^{-iE_i t} U^{\star}_{\beta i} |\nu_\beta(0)\rangle \tag{1.29}$$

$$= e^{-ipt} \sum_{i,\beta} U_{\alpha i} e^{-i\frac{m_i^2}{2p}t} U^{\star}_{\beta i} |\nu_\beta(0)\rangle \tag{1.30}$$

$$= \sum_{\beta} A_{\alpha\beta} |\nu_\beta(0)\rangle \tag{1.31}$$

where $A_{\alpha\beta}$ express the transition probability from ν_β to ν_α. The oscillation probability is calculated as

$$\mathcal{P}(\nu_\beta \longrightarrow \nu_\alpha) = |A_{\alpha\beta}|^2 \tag{1.32}$$

In the two flavor mixing case the calculation is rather simple and the mixing matrix has the form

$$U = \begin{pmatrix} \cos\theta & \sin\theta \\ -\sin\theta & \cos\theta \end{pmatrix} \tag{1.33}$$

As a consequence the oscillation probability is given by the relation

$$\mathcal{P}(\nu_e \longrightarrow \nu_\mu) = \sin^2 2\theta \sin^2 \left(1.27 \frac{\Delta m^2(eV^2) L(m)}{E(MeV)} \right) \tag{1.34}$$

where θ is the mixing angle, Δm^2 is the square mass difference of the two neutrino species, E is their energy and L is the distance traveled before a transition $\nu_\beta \to \nu_\alpha$ with probability $\mathcal{P}(\nu_\beta \longrightarrow \nu_\alpha)$.

1.4.3 Neutrino oscillations results

Neutrino masses and mixing constitute one of the outstanding problems of modern elementary particles physics.

In many laboratories around the world experiments designed to search for effects due to Majorana or Dirac masses and mixing of neutrinos are being performed.

The important parameters which define, in first approximation, the Δm^2 sensitivity of an experiment searching for neutrino oscillations, are L, the distance between neutrino production site and the detector, and p, the neutrino beam momentum. Typical values of such parameters for broad classes of neutrino experiments are given in table 1.2

Neutrino source	p (MeV)	L (m)	Δm^2 (eV^2)
Reactor	1	10^2	10^{-2}
Meson factory	10	10^2	10^{-1}
High energy accelerator	10^3	10^3	1
Atmospheric neutrinos	10^4	10^7	10^{-3}
Sun	1	10^{11}	10^{-11}

Table 1.2: Δm^2 *sensitivity for oscillation experiments with different neutrino sources.*

We shall brief summarize the results of ν–oscillation experiments in the following.

Atmospheric neutrino experiments
Atmospheric neutrinos are produced by the decay of pions and kaons generated when primary cosmic rays strike the upper atmosphere. The energy spectrum of these neutrinos peak at $\sim 1\ GeV$ and extends to several 100's of GeV. The neutrino flight distances vary from 15 km, for neutrinos produced at the zenith with respect to the detector, to 13000 km for neutrinos produced on the opposite side of the Earth, making measurements of atmospheric neutrinos sensitive to the neutrino oscillation parameter, Δm^2, at the level of $10^{-4}\ eV^2$. Basically, atmospheric neutrino experiments measure the flux of ν_μ and ν_e in a large sensitive volume and compare the observations to expectations based on detailed Monte Carlo simulations.

The "double ratio", defined as

$$R \sim \frac{(N_\mu/N_e)_{data}}{(N_\mu/N_e)_{MC}}$$

has been measured to be significantly lower than one in all high–statistic experiments observing atmospheric νs

This experimental observation along with other measurements (first of all the match between ν_e flux measured and expected), indicates ν_μ disappearance.

Solar neutrino experiments
Electron neutrinos are produced by nuclear reactions inside the Sun. Since the neutrino energy range extends from hundreds of keV to

15 MeV depending on the specific reaction producing the neutrino, and taking into account the distance between the Sun and the Earth is 1.5×10^8 km, the search for ν_e disappearance via solar neutrino detection is sensitive to oscillations for $\Delta m^2 < 10^{-11}$ eV^2. The detection methods are based on the counting of radioactive isotopes produced by the neutrino reactions, or on the measurement of $\nu_e + e \to \nu_e + e$ elastic scattering. All of the solar experiments have observed significant deficit in the solar neutrino flux compared with the Standard Solar Model.

Reactor experiments

At nuclear power reactors, electron anti–neutrinos are produced in the nuclear fissions of ^{235}U, ^{238}U, ^{239}Pu and ^{241}Pu with a mean energy of ~ 3 MeV. Anti–neutrinos are detected via the reaction $\overline{\nu}_e + p \to e^+ + n$. Detectors are typically placed at a distance from the reactor core varying from 10's of meters to 1 km.

The most sensitive reactor neutrino oscillation experiment, so far, has been the CHOOZ experiment. It has shown no evidence for spectral distortion, thus excluding a region in the oscillation parameter space down to 0.7×10^{-3} eV^2 at $\sin^2 2\theta = 1$ and $\sin^2 2\theta > 0.10$ at large Δm^2 regions.

Accelerator experiments

Neutrinos are produced at accelerators from the decay of pions produced by collisions of protons with a target. For proton beam energies in the range $1 \div 10$ GeV producing neutrinos of typical energies of 100 MeV and assuming distances from a neutrino source to a detector of the order of 1 km, the typical accelerator-based experiments sensitive is to $\Delta m^2 \sim 0.1$ eV^2.

The Liquid Scintillator Neutrino Detector (LSND) at the Los Alamos Meson Physics Facility has reported evidence for appearance of ν_e and $\overline{\nu}_e$ from pure beams of ν_μ and $\overline{\nu}_\mu$ with $\Delta m^2 \sim 1$ eV^2 and $\sin^2 2\theta \sim 10^{-2}$. The evidence for neutrino oscillations reported by LSND has not been confirmed. The KARMEN experiment also uses liquid scintillator to search for ν_e appearance from a ν_μ beam produced by muon decays at rest in a detector located at a distance of 17.7 m from the neutrino source. KARMEN has found no evidence for ν_e appearance above the expected background and excludes a region of oscillation

parameter space at the edge of the LSND allowed region.

Recently, support for the evidence of ν_μ disappearance in atmospheric neutrino experiments has been provided by the K2K experiment using a ν_μ beam produced at the KEK accelerator facility. This experiment compares fluxes of ν_μ in a near and a far detector (the latter being SuperKamiokande detector) located at a distance of 250 km. A sensitivity to the Δm^2 region indicated by atmospheric neutrinos is achieved given the neutrino beam energy available.

1.4.4 MSSM with right–handed neutrino

The see–saw mechanism[13] is the simplest model to generate the tiny neutrino masses. In this mechanism the Yukawa interactions are lepton flavor violating due to introduction of the right–handed neutrinos, similar to the quark sector, in full agreement with the solar and atmospheric neutrino oscillation observations. However, if the see–saw mechanism is added to the SM the effects of LFV in the charged lepton sector, induced by radiative corrections, are extremely small. On the other hand, large LFV effects can be expected if the supermultiplets of the right–handed Majorana neutrino are included in the SUSY model. In this way, the see–saw mechanism is conserved if the superpotential of lepton sector in the MSSM is given as

$$W = (y_e)_{ij} H_1 E_1^c L_j + (y_\nu)_{ij} H_2 N_i L_j + \frac{1}{2}(M_R)_{ij} N_i N_j \qquad (1.35)$$

where N_i is the right–handed neutrino supermultiplets, $(M_R)_{ij}$ is the Majorana mass matrix and $(y_\nu)_{ij}$ is a new Yukawa coupling constant matrix.

Since there are two Yukawa coupling matrices (y_e and y_ν) in the lepton sector, flavor mixing would arise and lepton flavor would be not conserved. The LFV effects are induced by the flavor mixing in left–handed slepton sector, through the renormalization effects from the Planck to the Majorana mass scale.

Chapter 2

$\mu \to e\gamma$ decay

The detection of Lepton–Flavor Violating processes would represent an important signal of new physics beyond the SM.

Among the various channels which might reveal LFV, those involving muon decays are the most appealing, due to the relatively easy production of high fluxes of low energy muon beams (about $10^{14} - 10^{15}$muons/year).

While, in the previous chapter the theoretical frameworks allowing for LFV have been presented, here we want to discuss in some detail, the phenomenology and the predictions for the $\mu \to e\gamma$ process. Moreover, in the last section, an overview of other muon LFV processes is presented.

2.1 $\mu \to e\gamma$ in the SM

As it is well known the lepton flavor changing processes are strictly forbidden in the Standard Model theory with $m_\nu = 0$. However, it is important to consider that radiative corrections can induce a rate different from zero for LFV processes.

Here, we want to illustrate the event rate calculation for the process $\mu \to e\gamma$ in the framework of the SM, with only one Higgs doublet, modified by the presence of neutrino mass terms and consequently ν mixing and oscillations. This calculation will show that, as expected, the LFV effects are very small due to the fact that they arise from radiation corrections which are further suppressed by factors $(m_\nu/M_W)^2$.

The lowest order diagrams contributing to the $\mu \to e\gamma$ amplitude in this renormalized gauge theory are displayed in fig.2.1. The exact calculation

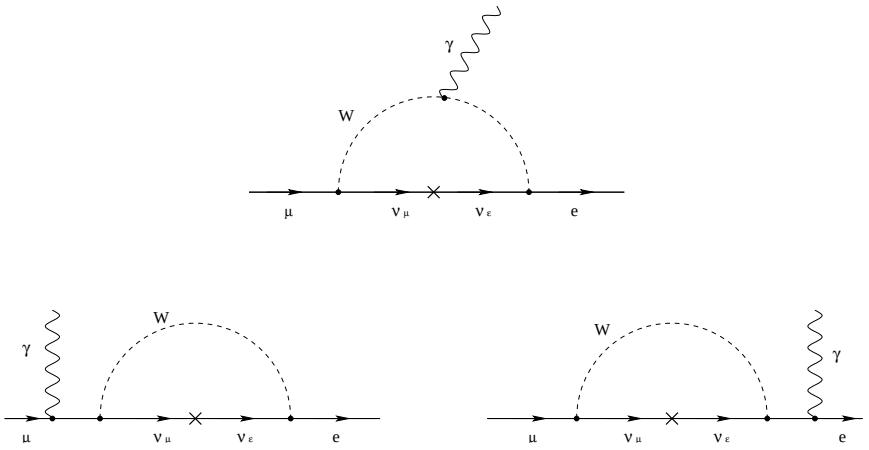

Figure 2.1: *One–loop diagrams for the $\mu \to e\gamma$ decay in the Standard Model*

[16] gives a transition rate

$$\Gamma(\mu \to e\gamma) = \frac{m_\mu^3}{8\pi}(|A|^2 + |B|^2) \tag{2.1}$$

where

$$A = B = \frac{eg^2}{8M_W^2}\frac{m_\mu}{32\pi}\delta_\nu \tag{2.2}$$

represent all contributions to Γ by radiative one loop diagrams. δ_ν is a sort of GIM suppression factor, coming from the unitary matrices describing the electron and muon neutrino flavor eigenstates in terms of mass eigenstates. Normalizing to the amplitude for the $\mu \to e\nu\bar{\nu}$ process, $\Gamma(\mu \to e\nu\bar{\nu}) = m_\mu^5 G_F^2/192\pi^3$, the branching ratio for the $\mu \to e\gamma$ process is

$$B.R.(\mu \to e\gamma) = \frac{\Gamma(\mu \to e\gamma)}{\Gamma(\mu \to e\nu\bar{\nu})} = \frac{3\alpha}{32\pi}\delta_\nu^2 \tag{2.3}$$

A rough evaluation of the transition rate for this process can be calculated using the results of solar neutrino oscillation experiments[17]. In this case, observing that the oscillation $\nu_\mu \to \nu_e$ should take place on a distance $L \sim 1/M_W$, that the energy flowing in the loop is of order M_W, the event rate can be factorized as

$$\Gamma(\mu \to e\gamma) = \frac{G_F^2 m_\mu^5}{192\pi^3}\frac{\alpha}{2\pi}\sin^2 2\theta \sin^2\left(\frac{1.27\Delta m^2}{M_W^2}\right) \tag{2.4}$$

The normalization to the Michel muon decay, gives a $B.R.(\mu \to e\gamma) = 10^{-55}$, that differs from the correct evaluation by a factor of 3/64.

2.2 $\mu \to e\gamma$ decay: SUSY–GUT prediction

As illustrated in §1.2 the SUSY extension of the SM has, in general, a large number of degrees of freedom which naturally lead to large LFV phenomena. The experimental evidence of very rare and small LFV processes is actually a strong constraint on the parameter space of the SUSY model. On the other hand, the assumption of the universality of masses and couplings at the SUSY breaking energy scale (usually refered as mSUGRA model) implies a drastic suppression of all LFV effects.

One way to account for small LFV effects in a minimal theoretical framework is to add to the mSUGRA extension of the SM a group of Grand Unification which describes a symmetry between leptonic and hadronic degrees of freedom at a energy scale, M_{GUT} (usually assumed of the order of 10^{16} GeV), smaller than the scale of supersymmetry breaking. In this way, a minimal set of new degrees of freedom of the theory can account for LFV via a simple mechanism, even without invoking ν masses: the flavor mixing of the SM quarks (described by the V_{CKM} matrix) is transmitted to the squark sector (via the SUSY symmetry) and, from there, to the slepton sector (via the grand unification symmetry group) in the energy region $M_{GUT} \leq E \leq M_{SUSYbreak.}$. Finally, SUSY allows this flavor mixing to be transmitted to the SM lepton sector.

The predicted phenomenology depends on the details of the model, in particular on the gauge grand unification group. In the following, we briefly describe the predictions for the $\mu \to e\gamma$ decay in the $SU(5)$ and $SO(10)$ grand unification models.

2.2.1 Prediction in $SU(5)$

If an effective theory is super–symmetric at scale $M_F \sim 100$ GeV, the LFV processes are suppressed by powers of M_F.
In the $SU(5)$ model, after the symmetry breaking, the decay amplitude for $\mu \to e\gamma$ can be written as[18]

$$\mathcal{A}^{\mu} = -i\frac{e}{m^2_{\tilde{\mu}}}\bar{u}_e \left(q^2 F_1' \gamma^{\mu} P_R + m_{\mu} F_2 i\sigma^{\mu\nu} q_{\nu} P_L\right) u_{\mu} \tag{2.5}$$

where q_ν is the 4–momentum of γ, m_μ the muon mass and $P_{L,R}$ the chirality projection operators.

The form factors receive contribution at one–loop from Feynman diagrams of the type shown in fig.2.2. In the limit of vanishing gaugino mass,

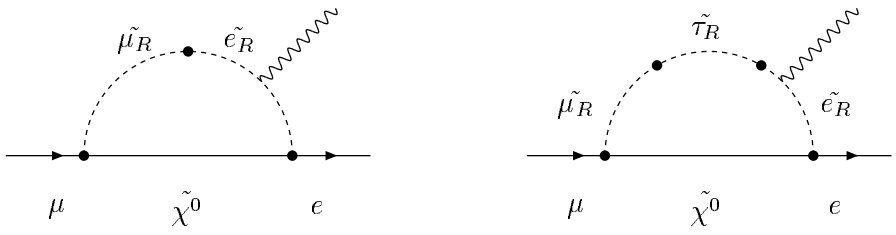

Figure 2.2: *Feynman diagrams in SU(5) SUSY–GUT for the $\mu \to e\gamma$ decay. The closed blobs represent the flavor transition due to the off–diagonal terms of the slepton mass matrices.*

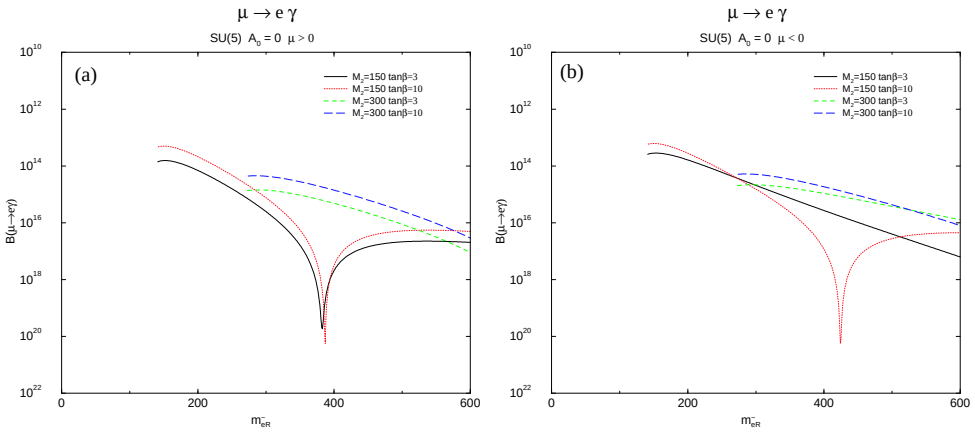

Figure 2.3: *Predicted B.R. for $\mu \to e\gamma$ decay in the SU(5) SUSY model as a function of the right–handed slepton mass for four different sets of the SUSY input parameters of M_2 (universal gaugino mass) and* $\tan\beta$.

partial width of $\mu \to e\gamma$ is

$$\Gamma(\mu \to e\gamma) = \frac{\alpha}{4}|F_2|^2 \frac{m_\mu^5}{m_{\tilde{\mu}}^4} \tag{2.6}$$

The corresponding branching ratios is

$$B.R. = 2.4 \times 10^{-12} \left(\frac{|V_{ts}|}{0.04}\frac{|V_{td}|}{0.01}\right)^2 \left(\frac{100\ GeV}{m_{\tilde{\mu}}}\right)^4 \tag{2.7}$$

with V_{ij} the measured value of the Kobayashi–Maskawa mixing matrix.

The prediction of the branching ratios of $\mu \to e\gamma$ decay, for a large parameter space region is presented in fig.2.3.

We notice that LFV in $SU(5)$ appears only in the right–handed slepton sector for a small or moderate values of $\tan\beta$, which is defined by the ratio of two Higgs vacuum expectation values. This is because the renormalization effects contribute only to $\tilde{e}_R$, and not to $\tilde{l}_L$. As a result, the helicity of

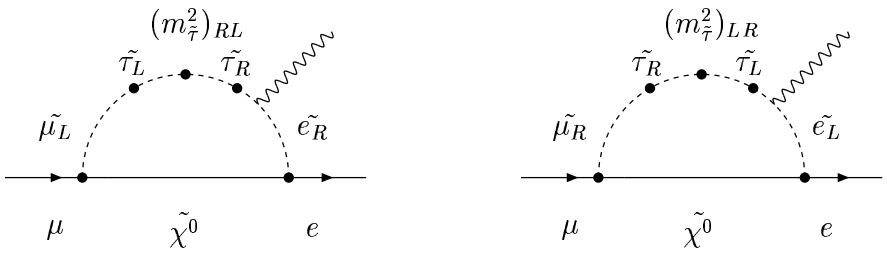

Figure 2.4: *Feynman diagrams in SO(10) SUSY–GUT which give dominant contributions to the $\mu \to e\gamma$. $(m^2_{\tilde{\tau}})_{RL}$ and $(m^2_{\tilde{\tau}})_{LR}$ are proportional to m_τ.*

an electron (positron) in LFV processes becomes only right–handed (left–handed). For instance, only $\mu^+ \to e^+_L\gamma$ decay occurs, not $\mu^+ \to e^+_R\gamma$. These two processes can be distinguished when the angular distribution of the $\mu^+ \to e^+\gamma$ signal is measured by using polarized muons. Moreover, the plots have been obtained with the followed CKM matrix values: $|V_{cb}| = 0.04$ and $|V_{td}| = 0.01$ and assuming valid the relation (1.19). This is based on the assumption that all of the Yukawa couplings are generated from the superpotential. However, it is known that this assumption does not yield a realistic mass relation for the down type quarks and charged leptons in the first a second generations. If higher dimensional terms or different $SU(5)$ representations of the Higgs fields are included to solve this problem, the simple relationship (1.19) would be lost. As a consequence, the predicted branching ratios could be different from those in fig.2.3.

2.2.2 Prediction in $SO(10)$

The Feynman diagrams contributing to $\mu \to e\gamma$ process in $SO(10)$ are shown in fig.2.4 In this model LFV processes are mediated by both the left and the right handed sleptons and a unique loop integral F, with dimensions of the inverse of a squared mass, gives the dominant contribution to all these processes.

The correct event rates calculation gives[19]

$$\Gamma(\mu \to e\gamma) = \frac{\alpha}{2} m^3_\mu |F|^2 \tag{2.8}$$

with F depending on the following low energy parameters:

- lepton–slepton mixing angle;

- the μ parameter and neutralino masses;

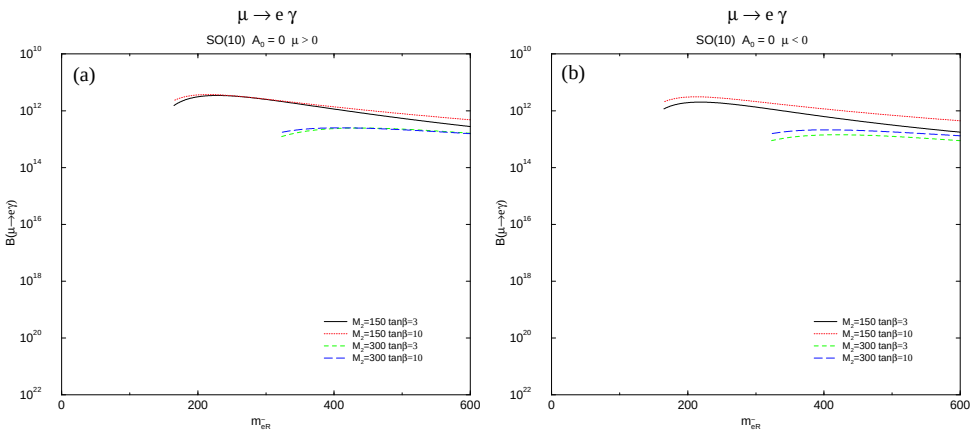

Figure 2.5: *Predicted B.R. for $\mu \to e\gamma$ decay in the SO(10) model.*

- the slepton masses.

Prediction for the branching ratio of $\mu \to e\gamma$ decay are shown in fig.2.5, while in fig.2.6 is plotted the B.R. as function of λ_G, a fundamental $SO(10)$ theory parameter, for $m_{\tilde{e}_R} = 1\ TeV$. The main result is that, in the large $\tan\beta$ region, the present experimental limits on LFV already constrain in a significant way the parameter space. Probably, the experiments in progress will be to able to probe the theory up to $\tilde{e}$ and $\tilde{\mu}$ masses of about 1 TeV and, eventually, to further constrain the parameters space.

2.2.3 Prediction in MSSM with RH neutrino

An alternative approach, as discussed in the previous chapter, is to generate slepton mixing from neutrino mixing, if R–handed Majorana neutrinos are added to the particle content of the MSSM.

The branching ratios for $\mu \to e\gamma$ can be evaluated by using the neutrino mixing parameter[20].
The model prediction are shown in fig.2.7, where the branching ratios is plotted as a function of the solar neutrino mixing: the predicted rate approaches the experimental bound for a Majorana mass larger than $10^{14}\ GeV$, if the large angle MSW solution for the solar neutrino problem is chosen.

2.3 $\mu \to e\gamma$ search

In this section we want to illustrate the advantages and the difficulties that arise in the LFV search in the muon decay to electron and photon.

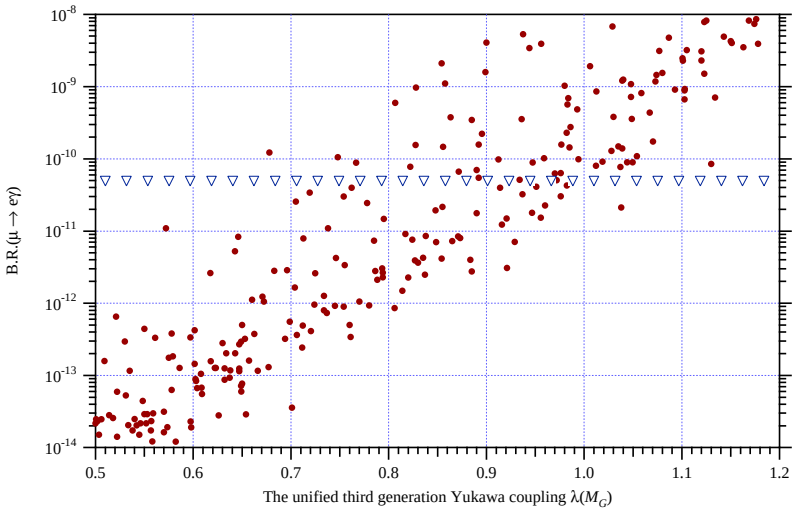

Figure 2.6: *$B.R.(\mu \to e\gamma)$ as function of λ_G for $m_{\tilde{e}_R} = 1\ TeV$ and acceptable values of the other free parameters. The line of $\bigtriangledown$ denotes the experimental upper bound.*

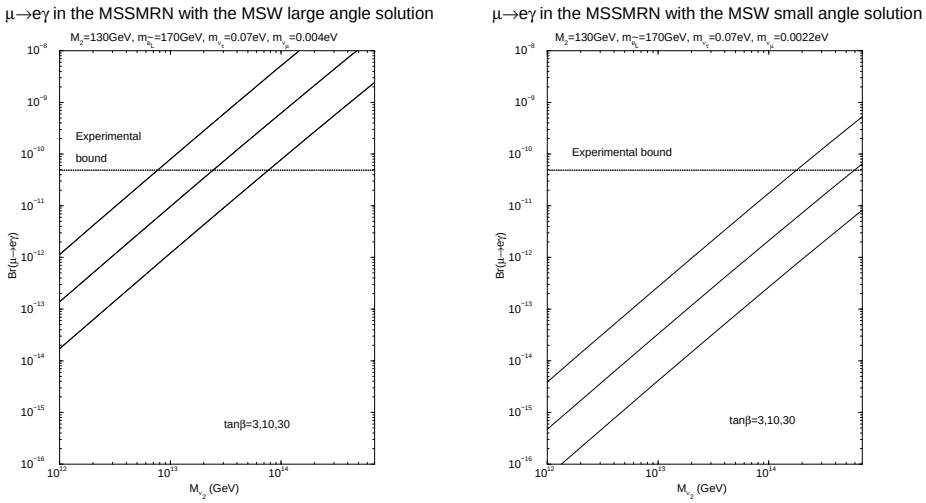

Figure 2.7: *Predicted branching ratios of $\mu \to e\gamma$ decay as a function of the Majorana mass of the second generation right–handed neutrino (M_{ν_2}) in the MSSM model with right–handed neutrino. They are given for the MSW large angle (left) and the MSW small angle (right) solution. The three curves correspond to $\tan\beta = 30, 10$ and 3 from top to bottom for both figures.*

2.3.1 Event signature

The main advantage of the $\mu \to e\gamma$ process is its clear signature: a *positron* and a *photon* in time coincidence, that are collinearly moving back–to–back, with energies equal to half of the muon mass ($m_\mu/2 = 52.8\ MeV/c^2$).

Of course there are two major background that contaminate the signal signature: one is a physics background (prompt), from the radiative muon decay ($\mu^+ \to e^+\nu_e\bar{\nu}_\mu\gamma$), the other is an accidental coincidence of an e^+ from a normal muon decay (Michel decay), with a high energy photon. The source the latter might be either a radiative muon decay, or a positron from normal muon decay which annihilate in flight, or an external bremsstrahlung photon.

2.3.2 Physics background

The differential decay width for the muon radiative decay ($\mu^+ \to e^+\nu_e\bar{\nu}_\mu\gamma$), was calculated, many years ago, as a function of the positron energy (E_e) and photon energy (E_γ) normalized to their maximum value ($E_{max} = m_\mu/2$)[21][22]. The branching ratio in this channel, as reported in the PDG[23], is 1.4% for $E_\gamma > 10\ MeV$.

In the limit of $E_e \approx E_{max}$ and $E_\gamma \approx E_{max}$ with an angle between the positron and photon ($\theta_{e\gamma}$) of about 180°, the muon radiative decay becomes an important background source to the $\mu \to e\gamma$ decay. In this case the differential decay width is given by[24]

$$d\Gamma(\mu \to e\nu_e\bar{\nu}_\mu\gamma) \cong \frac{G_F^2 m_\mu^5 \alpha}{3 \times 2^8 \pi^4} \left[(1-x)^2(1 - P_\mu \cos\theta) + \left(4(1-x)(1-y) - \frac{1}{2}z^2\right)(1 + P_\mu \cos\theta)\right] dx dy z dz d(\cos\theta) \tag{2.9}$$

where G_F is the Fermi coupling constant, α is the fine structure constant, P_μ is the muon–spin polarization and

$$\begin{aligned} x &= \frac{2E_e}{m_\mu} \\ y &= \frac{2E_\gamma}{m_\mu} \\ z &= \pi - \theta_{e\gamma} \end{aligned}$$

are the relevant kinematic parameters describing the process.

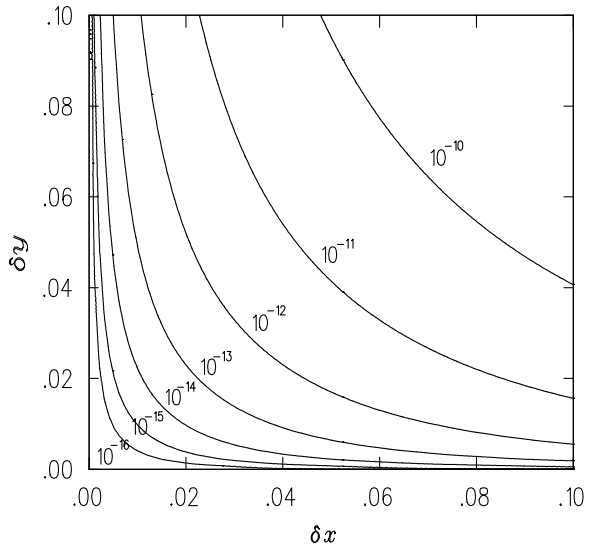

Figure 2.8: *Sensitivity limitation on the branching ratio of $\mu \to e\gamma$ imposed by $\mu \to e\nu\bar{\nu}\gamma$ decay for the case of unpolarized muons as a function of δx and δy.*

The decay width (2.9) plays an important role in the evaluation at the sensitivity for a $\mu \to e\gamma$ search. For $x = 1$ and $y = 1$ exactly (which correspond to the $\mu \to e\gamma$ signature), the differential decay width would vanish; however, as a result of the finite detector resolutions, configurations with x and y smaller than 1 mimic the signal kinematics and become a background source.

Therefore, given the detector resolutions, the sensitivity limitation from $\mu^+ \to e^+\nu_e\bar{\nu}_\mu\gamma$ background decay can be evaluated by integrating the differential decay width in (2.9) over a kinematic region determined by the detector resolutions[1] for signal events.

Fig.2.8 shows the sensitivity limit imposed by the $\mu \to e\nu\bar{\nu}\gamma$ decay of unpolarized muons as a function of the detector resolutions. In this calculation δx, δy and δz define the kinematic range of the signal region for e^+ energy ($1 - \delta x \leq x \leq 1$), that for photon energy ($1 - \delta y \leq y \leq 1$), and that for the angle of $z = \pi - \theta_{e\gamma}$ ($0 \leq z \leq \delta z$), respectively. It can be seen that, to achieve a sensitivity limit of a level of 10^{-15}, both δx and δy of the order of 0.01 are needed.

[1] The size of the signal region is generally assigned by a few times the rms of the detector resolutions in order to keep a high acceptance for the signal.

2.3.3 Accidental background

Another serious background to $\mu \to e\gamma$ is an accidental coincidence of a high energy e^+, from the normal muon decay, with a high energy photon.

The event rate of the accidental background normalized to the total decay rate (B_{acc}) can be estimated by

$$B_{acc} = R_\mu \cdot f_e \cdot f_\gamma \cdot (\Delta t_{e\gamma}) \cdot \left(\frac{\Delta\Omega_{e\gamma}}{4\pi}\right) \tag{2.10}$$

where:

R_μ is the instantaneous muon intensity;

f_e and f_γ are the integrated fractions of the spectrum of e^+ in the normal muon decay and that of photon within the signal region

$\Delta t_{e\gamma}$ and $\Delta\Omega_{e\gamma}$ are the full widths of the signal regions for timing coincidence and angular constraint of the back–to–back kinematics, respectively.

Given the sizes of the signal region defined by δx, δy and δz, it is possible to estimate f_e by integrating the Michel spectrum of the normal muon decay on the x range, and f_γ taking in account the contributions of all sources of high energy photons. Taking some reference numbers, such as the e^+ energy resolution of 1%, the photon energy resolution of 6%, $\Delta\Omega_{e\gamma} = 3 \times 10^{-4}\ str$, $\Delta t_{e\gamma} = 1\ ns$ and $R_\mu = 3 \times 10^8\ \mu/s$, the accidental background rate is equivalent to 3×10^{-13}.

This accidental background can be reduced by an improved timing resolution of the experimental apparatus. However, at high event rate, it is desirable to reduce this background by some additional method as, for example, using the polarized mouns beam where the angular properties of signal and background particles can be distinguished.

2.3.4 Muon polarization

The angular distribution of the positrons, from the $\mu \to e\gamma$ decay, with respect to the direction of muon polarization is very important because it would provide a way to discriminate among some theoretical models.

Moreover, the muon polarization is important in the background estimation too. We note as in the differential decay width, for muon radiative

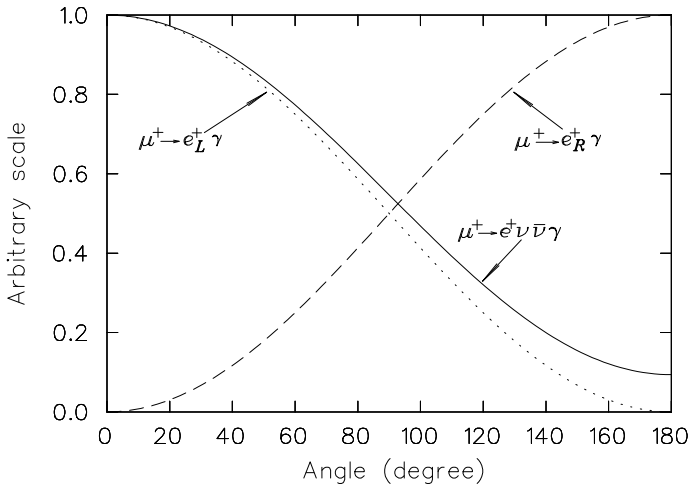

Figure 2.9: *Angular distribution of e^+s in $\mu^+ \to e^+ \nu \bar{\nu} \gamma$ decay (solid line). $\mu^+ \to e_L^+$ (dotted line) and $\mu^+ \to e_R^+$ (dashed line) decays are shown.*

decay (2.9), it is possible distinguish the term related to the positrons emitted opposite to the muon muon–spin direction (the first term), and the term for the positrons emitted along the muon–spin direction (the second term).

Again, the positrons from the normal muon decay, to the high energy ($x \approx 1$) are emitted along the muon–spin direction, following an angular distribution of $1 + P_\mu \cos\theta$[25][26].

Thus, the detection of positrons emitted opposite to the muon–spin direction would reduce the background contribution to the $\mu \to e\gamma$ decay. Of course, in this way, only the acceptance to $\mu \to e_R\gamma$ decay is kept high, since it follows a $1 - P_\mu \cos\theta$ angular distribution. The use of polarized or unpolarized muons will not make a difference in the detection of $\mu \to e\gamma$.

The angular distribution as calculated by[24] are illustrated in fig.2.9.

2.3.5 Experimental results

Experimental searches for $\mu \to e\gamma$ have a long history of more than 50 years. The principal experimental efforts have been devoted to improving the detection resolutions of the four variables, namely the positron and photon energies, the timing coincidence and the angle between the positron and the photon, through the use source and more refined experimental techniques.

In table 2.1, several experimental results of 90% C.L. upper limit of $\mu \to e\gamma$ decay obtained in the past experiments are listed along with the resolutions driving these results. The current upper limit, as quoted in the

Place	Year	ΔE_e	ΔE_γ	$\Delta t_{e\gamma}(ns)$	$\Delta\theta_{e\gamma}(mrad)$	Upper limit
TRIUMF	1977	10%	8.7%	6.7	-	$< 3.6 \times 10^{-9}$
SIN	1980	8.7%	9.3%	1.4	-	$< 1.0 \times 10^{-9}$
LANL	1982	8.8%	8%	1.9	37	$< 1.7 \times 10^{-10}$
LANL	1988	8%	8%	1.8	87	$< 4.9 \times 10^{-11}$
LANL	1999	1.2%	4.5%	1.6	15	$< 1.2 \times 10^{-11}$

Table 2.1: *Historical progress of search for $\mu \to e\gamma$ with 90% C.L. upper limit. The resolutions quoted are given as a full width at half maximum (FWHM).*

PDG, is

$$B.R.(\mu \to e\gamma) < 4.9 \times 10^{-11} \tag{2.11}$$

which was obtained by an experiment at Los Alamos National Laboratory (LANL), while a new experiment at PSI, that will be to discuss in the next chapter, aims to achieve a sensitivity of 10^{-14} in the $\mu \to e\gamma$ branching ratio.

2.4 Other LFV processes

2.4.1 $\mu^+ \to e^+e^+e^-$

In parallel to $\mu \to e\gamma$ decay, another very important muon LFV process is $\mu^+ \to e^+e^+e^-$.

Phenomenologically, the relevant terms in the LFV Lagrangian are the general four fermion couplings, while experimentally the event signature is a three particles final state. Kinetically, if the muon decays at rest, the particles detected must satisfy the momentum ($|\sum \vec{p}_i| = 0$) and energy ($\sum E_i = m_\mu$) conservation with the timing coincidence between two positrons and an electron.

The main difficulty in this channel is the copious pair production by photon conversion that is a very important background source and causes a loss of the signal sensitivity, in particular for theoretical models in which the $\mu^+ \to e^+e^+e^-$ decay occurs mostly through photonic diagrams.

Among the past experiments on the search for $\mu^+ \to e^+e^+e^-$, an important result has been achieved by an experiment carried out at JINR laboratory of Dubna (Russia)[27]. Using a magnetic 4π spectrometer with

cylindrical proportional chambers, it obtained an upper limit of 90% C.L. of

$$B.R.(\mu^+ \to e^+e^+e^-) < 3.6 \times 10^{-11} \tag{2.12}$$

2.4.2 μ^-–e^- conversion

Another prominent process concerning lepton flavor violation is μ^-–e^- conversion in a muonic atom. When a negative muon is stopped in some material, it is trapped by an atom and forms a muonic atom. In the context of physics beyond the SM, the exotic process of neutrinoless muon capture, such as

$$\mu^- + (A, Z) \to e^- + (A, Z) \tag{2.13}$$

is also expected. This process, called μ^-–e^- conversion, violates the conservation of the lepton flavor numbers (L_e and L_μ), but conserves the total lepton number.

From an experimental point of view, μ^-–e^- conversion is very attractive. In fact, it has a mono–energetic single electron emitted with energy

$$E_{\mu e} \approx m_\mu - B_\mu \tag{2.14}$$

where m_μ is the muon mass and B_μ is the binding energy of the $1s$ muonic atom, and no coincidence measurement is required. Moreover, since B_μ is different for various nuclei, the peak energy for the event signature changes with the material. For example, it varies from $E_{\mu e} = 104.3\ MeV$ for Ti to $E_{\mu e} = 94.9\ MeV$ for Pb, that is far above the end–point energy of the electrons for Michel decay of the muon spectrum ($\sim 52.8\ MeV$).

This process, as well as the charge – changing reaction, such as

$$\mu^- + (A, Z) \to e^+ + (A, Z-2)^\star \tag{2.15}$$

which violates the conservation the family lepton number too, was studied in the SINDRUM II experiment at PSI laboratory[28], using various nuclei; the main results are reported in table 2.2.

2.4.3 Muonium to anti – muonium conversion

A muonium atom (Mu) is a hydrogen–like bound state of μ^+ and e^-, that was observed for the first time at the Nevis cyclotron of the Columbia University in the 1960[29]. The spontaneous $Mu - \overline{Mu}$ conversion is another

Process	90% C.L. upper limit	year
$\mu^- + Ti \to e^- Ti$	$< 4.3 \times 10^{-12}$	1993
$\mu^- + Ti \to e^+ Ca(gs)$	$< 4.3 \times 10^{-12}$	1993
$\mu^- + Ti \to e^+ Ca(ex)$	$< 8.9 \times 10^{-11}$	1993
$\mu^- + Pb \to e^- Pb$	$< 4.6 \times 10^{-11}$	1996
$\mu^- + Ti \to e^- Ti$	$< 6.1 \times 10^{-13}$	1998
$\mu^- + Ti \to e^+ Ca(gs)$	$< 1.7 \times 10^{-12}$	1998
$\mu^- + Ti \to e^+ Ca(ex)$	$< 3.6 \times 10^{-11}$	1998

Table 2.2: *Results from SINDRUM II Collaboration at PSI on a search for $\mu^- - e^-$ coherent conversion and for $\mu^- - e^+$ conversion in muonic atoms. For the charge – changing process the transition to the ground state (gs) and excited states (ex) also are reported.*

class of muon LFV processes with $\Delta L = \pm 2$. Its phenomenology was studied by Feinberg and Weinberg[30].

In the experiments for this process, is searched an $\overline{Mu}$ from a muonium initially produced. The signature of an anti–muonium decay is the emission of an energetic e^- from $\mu^- \to e^- \bar{\nu}_\mu \nu_e$ decay with a dissociated e^+ left behind with an average kinetic energy of 13.5 eV.

The sensitivity to $Mu - \overline{Mu}$ conversion is suppressed when the muonium atom is embedded in matter, since a negative muon in the anti–muonium is easily captured by the surrounding atoms.

An experiment carried out at PSI laboratory in the 1999[31] has given a 90% C.L. upper limit on the conversion probability at zero magnetic field less than $8.3 \times 10^{-11}/S_B$, where S_B describes the suppression of the $Mu - \overline{Mu}$ conversion in an external magnetic field.

Chapter 3

The MEG experiment

When the muon was discovered, it was tough as a heavy electron that would also decay into an electron and a neutral particles as a γ–ray.

The first search for $\mu^+ \to e^+\gamma$ was made by Hincks and Pontecorvo in 1947 [32] using cosmic ray muons. This was also the first try to search for lepton flavor violation. Its negative result set an upper limit of less than 10% for this processes.

After many years, the artificial production of the muon beams at the accelerators allowed to improve this upper limit by almost four orders of magnitude leading to $B.R.(\mu^+ \to e^+\gamma) < 2 \times 10^{-5}$ [33]

The unobserved $\mu^+ \to e^+\gamma$ decay, led directly to the hypothesis of two neutrino [34], in which the neutrino coupled to the muon is different from that coupled electron.

The experimental verification of the two neutrino hypothesis, at the Brookhaven National Laboratory [35], introduced in the SM the concept of the separate conservation of lepton flavor, thus the processes like $\mu^+ \to e^+\gamma$ should be forbidden.

As discussed in the previous chapters, recently considerable interest in LFV processes has arisen based on supersymmetric extension to the SM, in particular supersymmetric grand unified theories, that predict a measurable $B.R.$ for LFV processes, and on the evidence for neutrino oscillations.

The experimental upper limits on LFV in the μ–decay, have been continuously improved at a rate of about two orders of magnitude per decade for about 50 years since the first LFV experimental search. The current limit in PDG (1.2×10^{-11} with 90% C.L.), has been obtenued in the MEGA experiment at LAMPF laboratory in 1999[36].

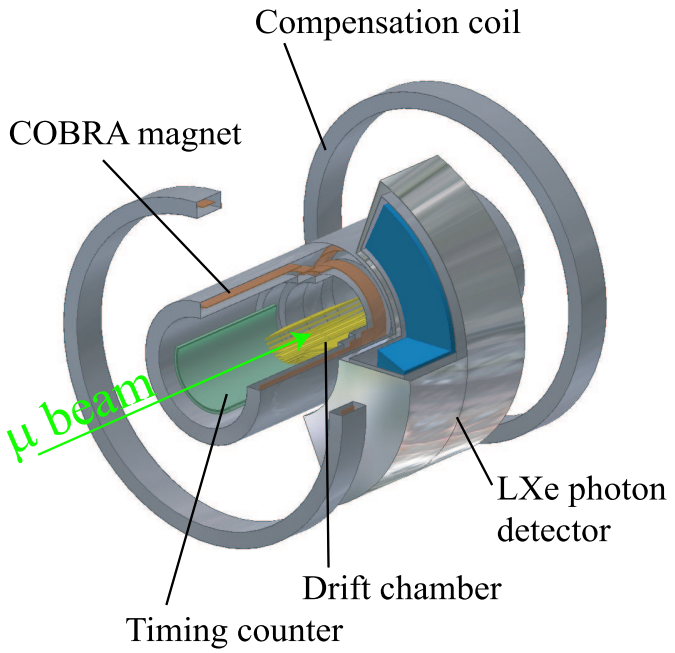

Figure 3.1: *Schematic 3D view of the MEG detector*

In the next years this result will be improved by the MEG experiment at the Paul Scherrer Institute of Zurich (CH), which will search the lepton flavor violating decay $\mu^+ \to e^+\gamma$ with a sensitivity of $\sim 5 \times 10^{-14}$.

3.1 The experiment at PSI Laboratory

The concept of the MEG experiment at the PSI laboratory is very simple: the detector is designed to identify pairs of positrons and photons in time coincidence, emitted back–to–back from the spot of a continuous muons beam stopped in a thin target. Figure 3.1 shows a schematic view of the MEG detector. The photon energy is measured in a Liquid–Xe scintillating calorimeter, while the positron track is reconstructed in a spectrometer, with inhomogeneous magnetic field. This later consists of a set of drift chambers to measure the positrons momentum, and a timing counter, to measure their time of flight. The solid angle covered by this configuration is about 10%.

Of course, the experimental challenge is the high efficiency and resolutions of the subdetectors needed to reach a sensitivity of 10^{-14} on the branching ratio (BR), as declared in the experiment proposal [37].

For a given value of the BR, the number of observed events can be

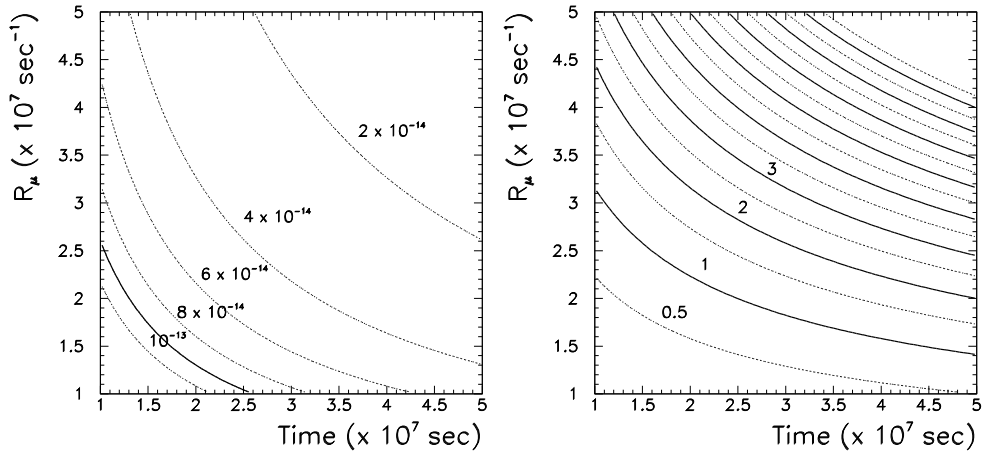

(a) (b)

Figure 3.2: a) *Single event sensitivity at* $\epsilon_\gamma = 0.65$ *as a function of the muon rate and of the running time.* b) *Number of expected background events as function of the muon stopping rate* R_μ *and measuring time* T.

written as follows

$$N_e = R_\mu T \frac{\Omega}{4\pi} \epsilon_e \epsilon_\gamma \epsilon_{cut} BR \tag{3.1}$$

with R_μ the muon stopping rate, T the total running time, Ω the solid angle covered by the detector and ϵ_e and ϵ_γ the detection efficiency for the positron and photon respectively. The ϵ_{cut} is the efficiency of the event selection, and it is depending on the detector resolution, since it takes into account the cuts applied on the reconstructed positron energy (E_e), photon energy (E_γ), opening angle ($\theta_{e\gamma}$) and relative timing ($t_{e\gamma}$).

Assuming 90% efficient cuts on the four parameters, the resulting selection efficiency, $\epsilon_{cut} = 0.66$, together a $\epsilon_\gamma \simeq 0.60$, a $\epsilon_e \simeq 0.90$ and $R_\mu = 0.3 \times 10^8/s$ imply that the minimum value of the BR allowing the detection of a single event in a total running time of 1 year (2.6×10^7 s), is about 4×10^{-14}.

The choice of the values of R_μ and T is a compromise between the need to perform the experiment in a reasonable time and to have a good single event sensitivity. The single event sensitivity is shown in fig.3.2.a as a function of the muon rate and of the running time. A comparison of this plot with that in fig.3.2.b shows that a reasonable choice, $R_\mu = 1.2 \times 10^7$ μ/s, $T = 3.5 \times 10^7$ s, yields a SES of 6×10^{-14}. It is clear that, due to the R_μ^2

dependence of the accidental background, for a given number of accepted background events it is more convenient to run for a longer time at a lower beam intensity, because the SES increases.

3.2 Beam and Target

3.2.1 The beam

The most stringent requirement to be met in order to improve the experimental limit for rare muon decays is the high intensity of the muon beam.

There are two types of the muon beams: pulsed and continuous beams. While in a pulsed beam the muons are grouped in bunches of definite time width, separated by a delay time in which the beam intensity is zero, so that the ratio between the bunch width and the total period defines the duty cycle of the beam, in a continuous muon beam the intensity is almost constant and the duty cycle is approximately equivalent to one. Therefore, for a given muon flux, the peak rate is higher in a pulsed beam with respect to a continuous beam.

For a $\mu^+ \to e^+\gamma$ search experiment, taking into account that the dominant background source, consisting of accidental coincidences, increases quadratically with the instantaneous muon rate, because the detected daughter particles comes from different muons, while the $\mu^+ \to e^+\gamma$ signal and the prompt background grows only linearly with the overall muon rate, the best choice is a continuous beam. In particular, the MEG collaboration has chosen the accelerator facility at the PSI laboratory, that is able to provide a beam intensity of $10^7 \div 10^8\ \mu^+/s$.

The PSI accelerator machine [38] generates a primary beam of protons that are accelerated by a ring cyclotron up to the energy of 590 MeV and then transported to two consecutive meson production carbon targets: M–target and E–target. The channel, labeled $\pi E5$, extracts low energy pion and muon beams from the tick production target at an angle of 175° with respect to the primary protons beam. The main characteristics of the beam are listed in table 3.1.

For the MEG experiment the beam channel will be tuned to $\approx 29\ MeV/c$ to collect muons with momentum well defined. Measurements, performed before starting the experiment, indicate that it is possible to have a beam intensity about of $1.3 \times 10^8\ \mu^+/s$ from a primary proton current of 1.8 mA

solid angle acceptance	150 msr
momentum range	$20 \div 120$ MeV/c
length	10.4 m
momentum band(FWHM)	10%
momentum resolution(FWHM)	2%
horizontal emittance	15.3 $cm \cdot rad$
vertical emittance	3.6 $cm \cdot rad$
spot size	4×4 cm^2

Table 3.1: *Main properties of the $\pi E5$ beam line.*

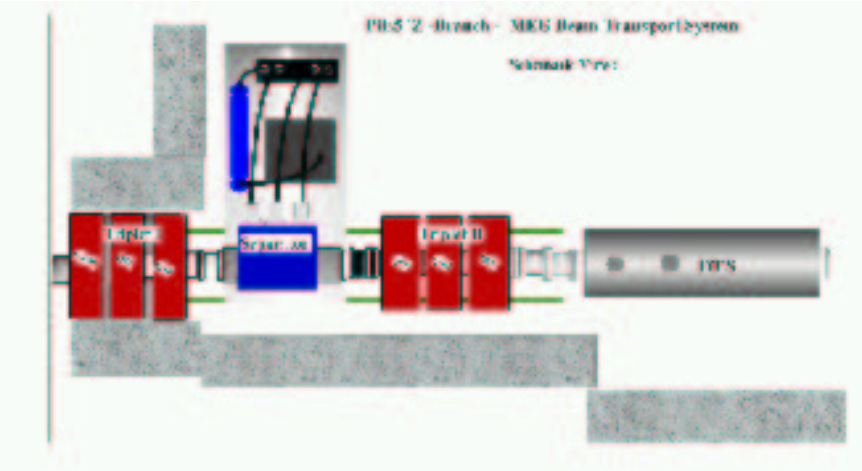

Figure 3.3: *Schematic view of the MEG beam line layout up to the injection into the COBRA spectrometer.*

[39].

Before to reach the MEG target, the beam must be manipulated in order to minimize the spot size and the momentum spread so that the muons can be efficiently stopped in a thin target, and in order to reduce the contaminant particles, mainly positrons in the beam.

The beam transport system, shown in fig.3.3, has been carefully designed [40] in order to reach the desired features of the beam at the entrance of the MEG experiment and it consist of four main components:

- the extraction element: it is a quadrupole triplet which couples the the $\pi E5$ channel to the experimental area;

Material	Density	Radiation Length	Mean Range 28 MeV/c	Target	Degrader
Mylar ($C_5H_4O_2$)	1.39 g/cm^3	28.7 cm	$\sim$ 870 μm	100 μm	600 μm
Polyethylene (CH_2)	0.95 g/cm^3	47.9 cm	$\sim$ 1100 μm	150 μm	700 μm
Kapton ($C_{22}H_{10}N_2O_5$)	1.42 g/cm^3	28.6 cm	$\sim$ 1100 μm	150 μm	700 μm

Table 3.2: *Comparison of material for the target.*

- the Wien Filter: an $E \times B$ crossed field, necessary for a good positrons suppression in the beam;
- Triplet II: a second quadrupole triplet which allows to have a good optical focusing at the collimator system placed behind this triplet;
- BTS (Beam Transport System) which is used as a coupling element to the spectrometer.

At the exit of the beam transport system we have, as lower limit, a beam intensity close to $1. \times 10^8$ μ^+/s [39] that is focused in a ellipsoidal spot whose axes measure $\sigma_x = 5.5$ mm and $\sigma_y = 6.5$ mm.

3.2.2 The target

The muon beam is stopped in a thin target which will be placed at the center of the spectrometer at a slant angle of 22° with respect to the beam direction.

Various materials have been scrutinized from the point of view of multiple scattering. The results are summarized in table 3.2. Assuming a central beam of 28 *Mev/c* the mean range is calculated to be $\sim$ 1100 μ/m for Polyethylene and Kapton, while $\sim$ 870 μ/m for other material. Supposing that it uses a 100 μm Mylar or equivalent thickness Polyethylene/Kapton, necessary thickness for degrader will be as shown in table 3.2. Note that the target will be places a slant angle, resulting in total thickness of the target and degrader smaller than mean range. Thus, overall, it seems that

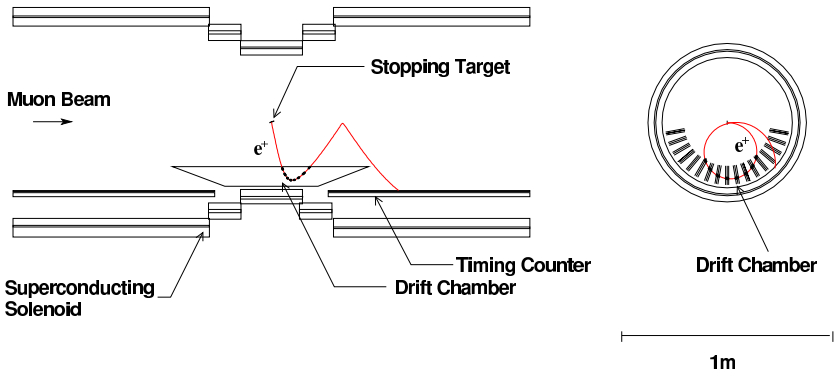

Figure 3.4: *Schematic view of the MEG spectrometer*

the Polyethylene is the best material for both as background suppression and beam quality (multiple scattering, or material amount) [41].

3.3 The Spectrometer

The COBRA (COnstant Bending RAdius) spectrometer is a positron detector consisting of a magnet specially designed to provide a gradient magnetic field, a drift chamber system to measure the positron momentum and a scintillation counter to measure their time of flight. Its schematic view is shown in fig.3.4

Before to discuss in detail each spectrometer component we introduce the reference frame. The coordinate system used is such that the z–axis lies along the incoming beam direction and the plane perpendicular to this direction is called r–ϕ plane. The origin of the reference system is the center of the target, which is placed at the center of the setup.

3.3.1 The superconducting magnet

The COBRA magnet consists of five superconducting coils of three different radii (a central coil, two gradient coils and two end coils), and a pair of compensation coils which are used to reduce the stray magnetic field around the photon detector (fig.3.5).

The cable winding of the superconducting coils is made of a Ni–Ti multi–filament wire embedded in a copper matrix, extruded in a rectangular aluminum box support of $1.2 \times 0.9\ mm^2$ of dimension.

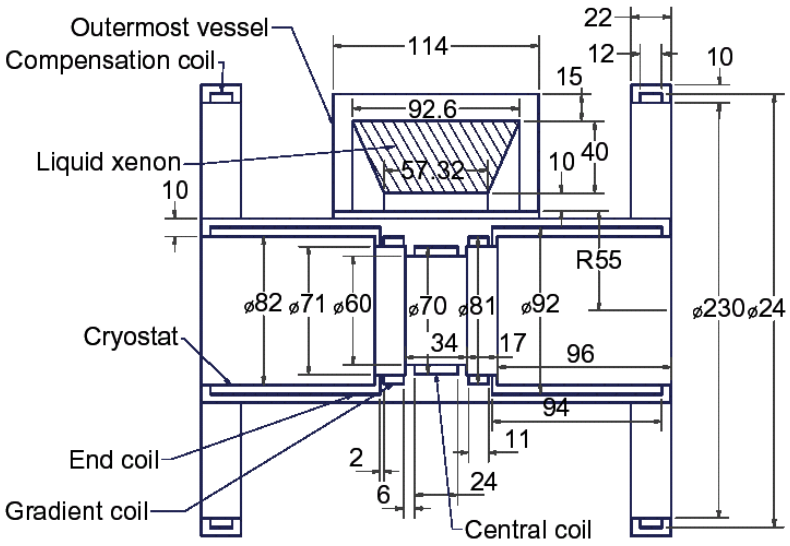

Figure 3.5: *A cross section view of the COBRA magnet.*

The superconducting coils are connected in series and the current density is controlled by changing the density of the cable winding and operating current.

The compensation coils, which have radii of 120 *cm* and are placed at both extremities of the COBRA magnet (see fig.3.1), are made of a resistive material. They allow to reduce the intensity of the magnetic field in the calorimeter region, thus avoiding to degrade the performances of the photodetection devices.

The special design for the magnet, moreover, allows to obtain a longitudinal magnetic field with intensity slowly decreasing with $|z|$. This configuration has the advantage of minimizing the occupancy of the drift chamber system which is particularly important given the high rate of events expected in MEG. While in a simple uniform solenoidal field, positrons emitted at a polar angle close to 90° make many turns in the tracking chambers (fig.3.6.a), causing problems in pattern recognition or even disturbing a stable operation of the chambers, in the solenoidal gradient field of COBRA those positrons are swept away much more quickly (fig.3.6.b). Moreover, in a uniform solenoidal field the bending radius of positrons of a given absolute momentum depends on the polar production angle (fig.3.6.c). On the other hand, the gradient field can be arranged, in such way, that monochromatic

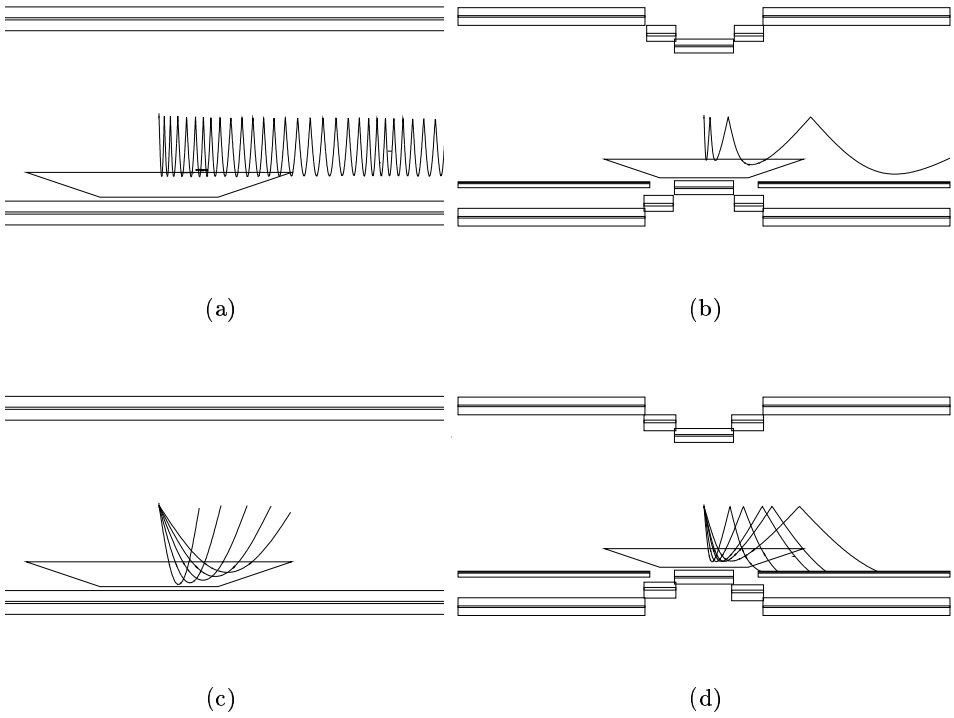

Figure 3.6: (a) *Trajectory of a particle that is emitted at* 88°*: it make many turns inside the detector in a uniform solenoidal magnetic field.* (b) *Trajectory of the same particle emitted at* 88° *inside of the COBRA spectrometer.* (c) *Trajectories of monochromatic particles emitted at various angles in a uniform solenoidal magnetic field: the bending radius depends on the emission angle.* (d) *Trajectories of monochromatic particles emitted at different angles inside the COBRA spectrometer: the bending radius is independent of the emission angle.*

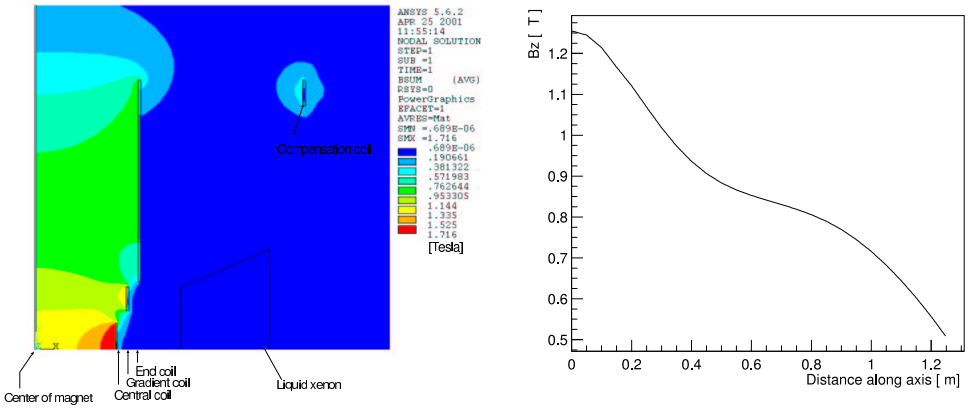

(a) (b)

Figure 3.7: a) *Contour plot of the magnetic field produced by the COBRA magnet;* b) *magnetic field intensity along the magnetic axis.*

positrons from the target follow trajectories with a constant projected bending radius independent of the emission angle (fig.3.6.d). As a consequence, it is possible to define the absolute momentum acceptance of positrons to be detected by the drift chamber system.

The contour plot and the profile of the magnetic field along the axis of the magnet is shown in fig.3.7. The maximum value of the field, in the central region is 1.25 $Tesla$, while at the ending of the drift chamber system the intensity is reduced by more than 30%.

3.3.2 The drift chambers system

The positron detector is a set of planar drift chambers arranged radially at 10° intervals in azimuthal angle and placed at a distance of 20 cm from the origin of the reference frame.
Each chamber consist of a pair of staggered drift cells arrays, and has a trapezoidal shape with length, along the longitudinal axis of 100 cm at the innermost radius and 44 cm at the outermost radius, and a width, in the radial direction, of about 9.5 cm. The chamber thickness is 1.5 cm[1].

The drift chamber geometry allows to detect the tracks associated to positrons with a momentum of 52.8 MeV/c that are emitted from the target

[1]The geometry described is those used by the Pisa simulation code and it is different from the geometry described in the proposal of the experiment [37].

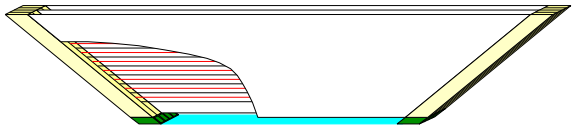

(a)

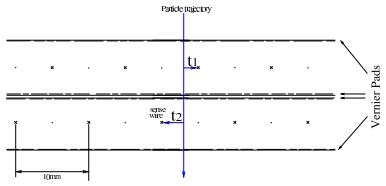

(b)

Figure 3.8: (a) *A longitudinal view of the drift chamber.* (b) *Cross–section view of a chamber sector. Showing the relative position of sense and field wires.*

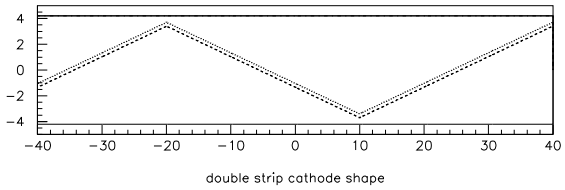

Figure 3.9: *Shape of the aluminum coating of the cathode foils (Vernier pads).*

with angles in the range:

$$|\cos\theta| < 0.35 \text{ and } -60^\circ < \phi < 60^\circ.$$

The chamber envelop is made of a thin plastic foil (12 μm of Kapton). The lateral walls are covered by a thin aluminum deposit, which is shaped with a Vernier pattern, in order to obtain the cathodic strips, whose relative width is a function of z (periodic). Several configurations have been considered over the years; the final design, which foresees two pads for drift cell, as shown in fig.3.9, should allow to determine the longitudinal position (z–coordinate of the hit) with an accuracy of about 300 μm [42] from the ratio of the signals induced on the two pads, thus improving the measurement obtained with the charge division method on the sense wire by a factor $\simeq 30$.

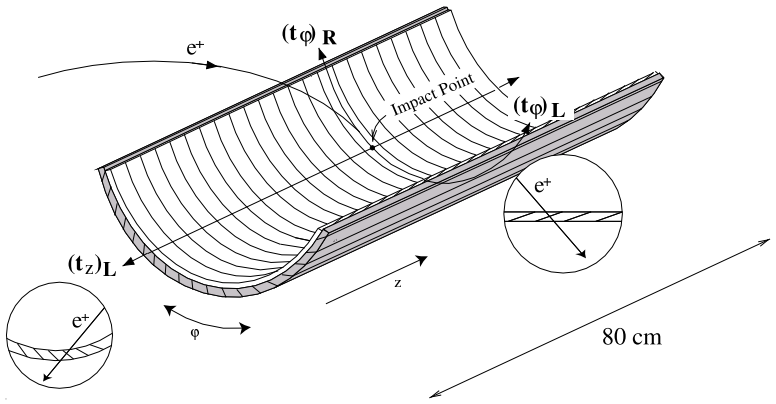

Figure 3.10: *The timing counter configuration.*

The chamber volume is filled with a 50%He – 50%C_2H_6 gas mixture at the pressure of 1 atm. Such mixture has been chosen because it guarantees a sufficient ionization production in small thickness of gas ($\sim 55\ e^-/cm$ for minimum ionizing particles) as well as a low multiple coulomb scattering for low momentum tracks (the radiation length is about 650 m) [43][44]. Moreover, the drift velocity saturates at roughly 3 $cm/\mu s$ for a relatively low electric field ($\sim 1.5 kV/cm$) [45].

The estimate accuracy, as coming out by preliminary test on the drift chamber prototype [46], is $100 \div 150\ \mu m$ for the radial position, and $5 \div 12\ ns$. They, should be sufficient to achieve a momentum resolution ranges from 0.7% to 0.9% FWHM on positrons of 52.8 MeV/c.

3.3.3 The Timing Counter

The main purpose of the timing counter detector (TC) is to provide the time o flight for positrons at the end of their path through the drift chambers. However, the MEG TC has been designed in such a way to provide a good spatial resolution so that it can be used for a rough estimation of the positron direction to be used for triggering purposes.

The TC is a hodoscope consisting of two arrays of plastic scintillators placed on both sides of the positron spectrometer, at a radius of $\sim 30\ cm$ and extending from $\varphi = 198°$ to $\varphi = 342°$ and $25 < |z| < 95\ cm$.

The $\mu^+ \to e^+\gamma$ positrons emitted in the angle range $0.08 < |\cos\theta| < 0.35$ will impinge on the detector after completing about 1.5 turns in the spectrometer volume.

Fig.3.11 shows the configuration of the timing counter which consists of

two layers of plastic scintillator bars. The outer layer, made of longitudinal bars, is used for timing measurements, while the inner layer, made of $5 \times 5\ mm^2$ scintillating fibers arranged in azimuthal bunches, is intended mainly for triggering purpose. The scintillator bars which compose the outer layer have a slant shape so that a positron incident on the hodoscope crosses two or three adjacent bars. The pulse–height ratio among these adjacent bars allows to refines the measurement of the impact point, with a limited granularity.

Moreover, the scintillation light is read–out on each side of the bars by PMTs, which measure the pulse–height as well as the arrival times of the signal (t_L and t_R) at both ends. The charge and time difference, $(q_L - q_R)$ and$(t_L - t_R)$, provide independent measurements of the impact point, while the mean time, $(t_L + t_R)/2$, provide an estimation of the absolute timing.

Test performed with cosmic rays and electron beams give a timing resolution of 100 ps FWHM [47][48] dominated by detector resolution, which exceed by a factor larger than two the time spread due to multiple coulomb scattering.

3.4 The Photon Detector

The success of the MEG experiment relies on the possibility to measure the photon four–momentum with very high precision.

The concept of photon detector adopted is similar to that of the "kamiokande" experiment: a sensitive volume whose outer surface is fully instrumented with 800 photo–multipliers. In particular, the MEG photon detector is a C–shaped homogeneous liquid–Xe scintillating calorimeter with a volume of $\sim 0.8\ m^3$, placed outside the COBRA magnet as shown in fig.3.3. The innermost detector surface is at 65 cm from the target center, just behind the superconducting coils of the COBRA spectrometer. Its thickness is 47 cm; the solid angle coverage is $\frac{\Delta\Omega}{4\pi} = 12\%$, for an extension of 120° in φ and for $|\cos\theta| < 0.35$. The light structure of the coil in front of the calorimeter assures that photons of 52.8 MeV reaches the calorimeter with a 95% probability.

The L–Xe choice is due to either its high light yield (comparable to NaI), which entails high efficiency and good energy resolution that its fast signal response. In particular, a fast signal formation is essential in order to have a precise timing of the measurement and, as a consequence, a minimal impact

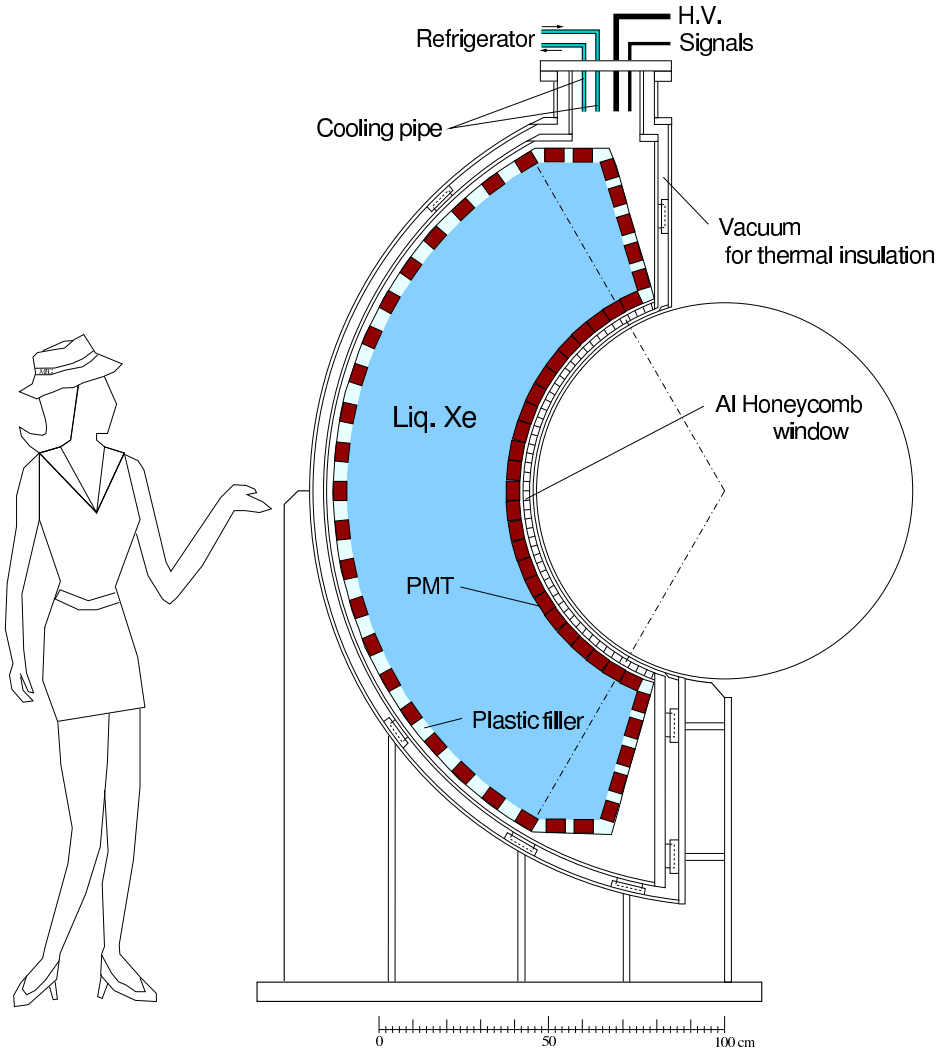

Figure 3.11: *Schematic view of the Liquid–Xe photon detector.*

Density	2.95 g/cm^3
Boiling and melting points	165 K, 161 K
Energy deposition per scintillation photon	24 eV
Radiation length	2.77 cm
Decay time (recombination)	45 ns
Decay time (fast component)	4.2 ns
Decay time (slow component)	22 ns
Emission peak	178 nm
Spectral width	14 nm
Refractive index	1.56
Absorption length	> 100 cm
Scattering length	29 cm to 50 cm

Table 3.3: *Properties of Liquid Xenon*

of the pile–up of accidental γ–rays under high rate background. Moreover, L–Xe is not effected by non–uniformity problems, which usually limit the energy resolution of scintillating crystals. The main properties of the LXe are summarized in table 3.3.

The detector is operated as a pure scintillation device (no ionization collection is performed) based on the collection of the ultraviolet light emitted by radiative transition of excited Xe atoms produced by ionizing radiations in the electromagnetic showers [49]. The formation of a "excimer–like" state, before the radiative decay, produces an emission peak (at 178 nm in L–Xe), separated enough from the absorption peak of the material which it makes them transparent to its scintillation light. Of course, the quality of the energy measurement and of the determination of the conversion point depend on the transmission of the emitted photon through the detector itself. If, one introduces the quantity λ_{att}, that takes in account both the real absorption and the photon elastic scattering one, the light attenuation in L–Xe can be parametrized as:

$$I(x) = I_0 e^{-x/\lambda_{att}} \tag{3.2}$$

Some studies of L–Xe properties have shown that λ_{att} is drastically affected by impurities of the medium [50]: the presence of a few parts for millions of substances, like H_2O or O_2, can change the optical parameters of L–Xe.

Therefore, the operation of the calorimeter requires of a purification and

a monitoring system of the L–Xe running continuously.

The detector is housed in a light stainless steel cryostat consisting of a Xe vessel and a vacuum vessel for thermal insulations of the liquid gas requiring a temperature of $-100°C$.

The scintillation light in the photon detector is collect by ~ 800 photo-multipliers (PMTs) located on the whole surface of the calorimeter envelop, which are read with a high precision and fast waveform digitizer (2.5 GHz).

From a weighed average of the light collection on the PMTs, the γ impact point is generally reconstructed within $\sim$ 5 mm in the transverse plane leading to a an angular resolutions for the flight directions of the γ of about 6.4 $mrad$. In the extreme case where the photon converts very close to the entrance of the calorimeter (at a depth < 1 cm) a resolution of about 10 $mrad$ is achieved in spite of the signal loss through the calorimeter front surface.

The absolute timing is estimated with a FWHM resolutions of about $100ps$.

The energy release for photon of 52.8 MeV/c is measured, from the sum of the signal from all PMTs, with a resolution (FWHM) of 1.4%. Lower energy measurements, leading to a long but tiny tail, are due to interactions of the photons with materials in front of the L–Xe, magnet, PMTs and their supports, calorimeter cryostat, which overall are 90% transparent to γ from $\mu^+ \to e^+\gamma$ decay. Early γ interactions result in a loss of efficiency, rather than a worsening in resolution, since only photons with energy measurements within a given cut will be accepted; as an example, a 2% cut in energy leads to an efficiency of 73%.

Photon pile–up will be rejected thanks to both the good energy capability of the MEG calorimeter, and the fine time sampling of the PMTs signals. From Monte Carlo studies, two photons with $E > 2.5$ MeV/c can be resolved in time if $\Delta t > 10$ ns and in space if their impact points are separated by more than 15 cm for $E > 5$ MeV/c.

To study the calorimeter performances, the collaboration has built a calorimeter prototype, with a sensitive volume of $40 \times 40 \times 50$ cm^3 equipped with 264 PMTs. The tests performed, using different sources, as cosmic rays, electron beams and α–particles, give a resolution on the γ–ray conversion point of $\sigma_{x,y} \sim 5$ mm. The absolute time resolution is $(105 \div 130)$ ps FWHM, that is comparable with the timing counter resolution. To concern the energy measurement, it is related to the distribution of the total PMT

charge, and it is depending on the cuts adopted in the reconstruction step. Any way, it is not great than 5% FWHM for positrons of 52.8 MeV/c. For more details on the prototype tests see [17].

3.5 Trigger and Data Acquisition

The trigger system of the MEG experiment is based on a fast digitization (the clock frequency is 100 MHz) of the LXe and timing counter PMT signals, and on the subsequent treatment of the digitized signals by means Field Programmable Gate Arrays (FPGA) that allow to perform an on–line individual correction of the PMT signal, as pedestal subtraction and common noise rejection. The Level1 trigger does not use the drift chamber which gives a slow response compared to L–Xe and TC.

The photon energy is determined by the sum of the light collect by all PMTs, while its direction is determined by the position of the PMT with the largest signal. Assuming a μ stopping rate of $R_\mu = 10^8\ \mu^+/s$ the rate of energy deposition above 45 MeV/c is about 2 kHz (this value is comprensive of the background photon rate).

The requirement of a positron tracks in time coincidence is tested by the timing counter. The back–to–back topology of the γ from $\mu^+ \to e^+\gamma$ events reflects into a well defined mapping of the photon impact point onto a specific region of the positron timing counter.

The overall rate in the timing counter due to Michel positron is estimated to be $R_{TC} \simeq 2\ MHz$. However the segmentation of the detector allows to implement in the trigger logic the back–to–back requirement which introduces a rejection factor $f_\phi \simeq 5$.

Thus, if we use a time coincidence window of $\Delta t = \pm 10\ ns$ between L–Xe and TC, the trigger rate due to uncorrelated background is

$$R = 2\Delta t R_\gamma \frac{R_{TC}}{f_\phi}\left(\frac{R_\mu}{10^8}\right) \simeq 20\ Hz \tag{3.3}$$

The estimated trigger rate is quite low compared to the present day DAQ and storage capabilities. This gives some margin in case of possible contributions not taken in account and/or of inclusion of calibration triggers during the normal runs.

For the data acquisition and storage, the experiment will use the MIDAS DAQ system [51], which has been successfully used in the past experiment at

PSI. The data rate depends on the trigger rate and the waveform compression in the front end electronics. Assuming an overall trigger rate of 100 *Hz*, which takes into account, along with the physics irreducible rate, either trigger streams for calibration and trigger streams for background analysis, and assuming that the data volume is dominated by the calorimeter output, i.e. 1.2 *MByte/event* data acquisition rate is 100 *MByte/s*.

Chapter 4

A Software Framework for the MEG Offline: MegRoot

The Software Offline System of an experiment consists of a set of software tools which are performing the different task necessary for the overall data processing required. In this chapter, a prototype for an offline software system, especially designed for the MEG experiment, will be described. This software, called MEGROOT and based on the ROOT [52] package, has been developed during year 2005 by the Lecce component of the collaboration. It is an Object Oriented system with all the needed user functionality, from data taking to final plot, in the ROOT framework. The choice of the ROOT environment is due mainly to the possibility of having a flexible data structure based on the TTree ROOT objects, which allow an easy access either to the full set of correlated data (i.e. a set of event data), or to only one or more sub–sample of the data structure, like, for example, data corresponding to a single sub–detector.

MegRoot is inspired to the offline software of the ALICE experiment (AliRoot) [53], from whom it inherits the architecture. The framework is flexible enough to allow the development of code for various purposes, from simulation to final data analysis, including the management of the detector geometry, the sub–detector response, the digitization and reconstruction steps, etc. The software suite consists of a set of C++ classes that are compiled against the ROOT utility library and loaded in the ROOT framework for any further data processing or analysis job.

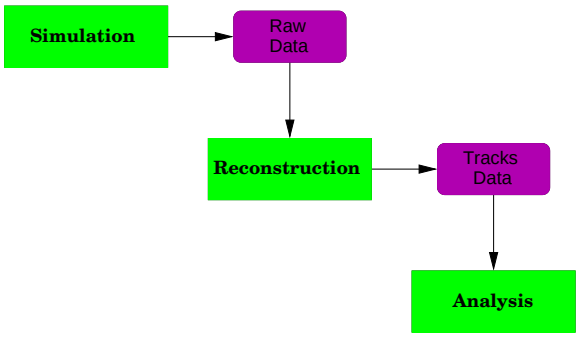

Figure 4.1: *General Architecture of MegRoot framework.*

4.1 The MegRoot Architecture

The Offline System must be able to manage the whole data processing of the experiment. Before the real run takes place, extensive simulations must be performed in order to test and commission the offline software. In particular, data simulated in the several steps of event generation, particle transport and modeling of the detector response, must be manipulated and transformed into a data format compatible with the real data read out in each subdetector; in this way, they can be used as input to check the reconstruction procedures and to measure the efficiency for signal selection. Fig.4.1 shows a simple schema of the general architecture of MegRoot framework, with the main components: *Simulation, Reconstruction* and *Analysis.*

Although the framework is subdivided in only three big block, its high modularity level is guaranteed by an independent implementation of the simulation and reconstruction steps for each subdetector. In this way, we define the detector base class (Detector Class) which is responsible to build the geometry of the detectors, to support both the hit and digit trees produced by the simulation step, but also the objects coming out from the reconstruction procedure.

The modularity of the algorithms reflects itself into a structured data model implemented as hierarchical folders. In particular, the ROOT environment, offers the tool of the ROOT folders, which can contain any kind of objects, can include other folders, etc., and allow easy access either by program or by the ROOT browser.

The main advantage, of ROOT folders is that they are organized in two main categories:

- data folders;

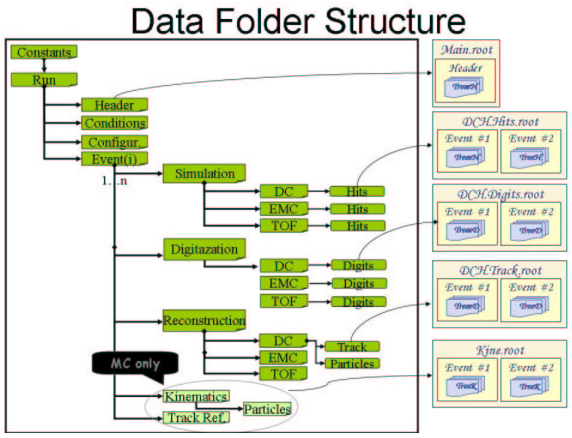

Figure 4.2: *The data folder structure.*

- task folders.

The *data folders*, whose the structure is shown in fig.4.2, contain constant data and event data. We can see as these contain the run sub–folder, that, itself, contains an event sub–folder for each event collected in the run. The event folder contains itself the following kind of data:

- raw data folder;

- reconstructed data folder;

- an extra folder with kinematics and other track references, in case of Monte Carlo data.

This data structure is shared by all subdetectors, i.e. all data folder is organized as sub–folders corresponding to the different subdetectors.

The *task folders* contain the actions, or the methods, that can be performed on the data by the detector modules. The main tasks are:

- *Reconstruction*: it performs the reconstruction of the subevent in the specific subdetector.

- *Data Quality Monitor*: it checks the quality of the subevent by a fast reconstruction and it fills the histograms that are part of the event and can be accessed at any stage of the data dataflow for quality assurance.

- *Calibration*: processes the subdetectors data to extract calibration constants to be used in subsequent reconstructions or monitoring tasks

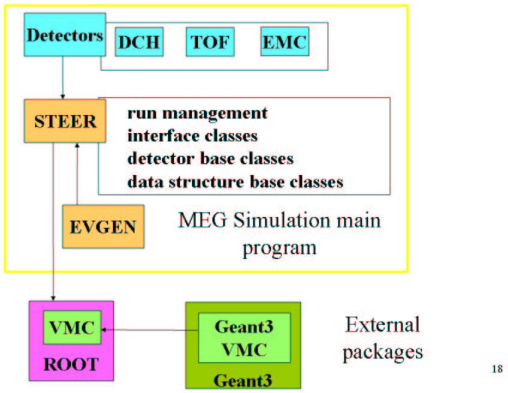

Figure 4.3: *Architecture of the simulation step in MegRoot.*

- *Alignment*: computes the alignment constant for the particular sub-detector.

- *Trigger*: it allows the simulation of the signals produced in each sub-detectors for the trigger system.

The coordination of the various tasks and the management of the data is performed by the *RunManager* object.

4.2 Simulation in MegRoot

The simulation in MegRoot consists of the event (physics) generation, particle transport and detailed detector response simulation. Its main components are the Virtual Monte Carlo, the detector classes, containing code specialized for experiment and a set of collaborating classes for particle simulation. A schematic view of the MegRoot simulation step is shown in fig.4.3

The main module, STEER, provides the interface classes for the detector description and data structures. It also provides the run steering functionality and it gives access to the collection generated particles when required by the Virtual MC. The run steering communicates with the event generator module via the interface class MegGenerator, with the specific detector modules via the MegDetector class, and with the transport MC via the Virtual MC main interface class, TVirtualMC.

The user code is structured according to the different sub–detector, taking into account that any dependence between sub–detector modules is forbidden.

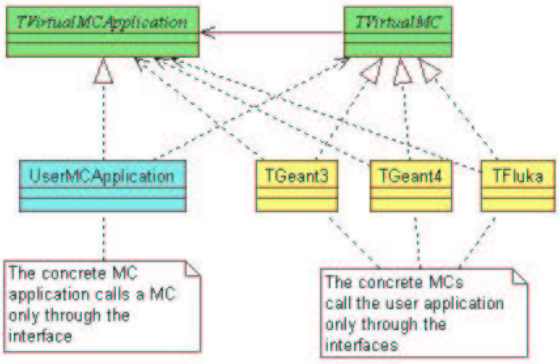

Figure 4.4: *The Virtual Monte Carlo design.*

4.2.1 The Virtual MC

The concept of Virtual Monte Carlo (VMC) has been developed by the ALICE Software project [55] to allow different Monte Carlo simulation programs to run without changing the user code, such as geometry definition, the detector response emulation or input and output formats. In this way it is possible to completely decouple the user code from the concrete MonteCarlo. A great advantage is that the geometry can be described independently from the transport MC and used also for reconstruction and visualization purposes.

The VMC structure, shown in fig.4.4, is based on the TVirtualMC, TVirtualMCApplication and TVirtualMCStack classes defined as a generalization of Geant3 functions and integrated in the ROOT framework.

The TVirtualMC class contains

- methods for building and accessing geometry;
- methods for accessing materials;
- methods for setting physics processes;
- methods for accessing transported particle;
- methods for run control.

The TVirtualMCApplication class contains the actions (implemented by the user) that can be performed during the simulation run

- build geometry;

- init geometry;

- begin event;

- stepping;

- finish event.

The TVirtualMCStack class defines the interface to a user defined particle stack.

The class methods are already developed and a user can access them by initializing a TVirtualMC object.

4.2.2 Event generator

The *Event Generator* is a builder of physics events that will be simulated in the MC programs, in other words it generates all particles involved in the physics process that afterwords will be transported by MC program in the detector.

The generators in a VMC are external packages, like *Pythia*, *Fluka*, or user defined generators, and the user can choose among them at runtime.

Since in the MEG experiment both signal and background events come from simple physics and have a clear kinematics, the choice of a user defined generator has been done in MegRoot.

The interface between VMC and event generator is provided by MegGenerator class, that provides the user also with a set of tools for testing and for performing background studies. Moreover, it allows to simulate a single process or a mixture of physics channels. In the latter case the interface uses the MegCocktail class, that collects a list of MegGenerator type objects.

Actually, in MegRoot three different user generators have been implemented:

- MegGenSignal: is the base class to define the signal event (a positron and gamma particle emitted back–to–back with energy of 52.8 MeV/c);

- MegGenPositron: is the base class to define positrons from Michel decays;

- MegRadDecay: is the base class to define the radiative decay.

4.2.3 The geometry

The detector geometry is based on the Geant3.21 [54] package. In particular, MegRoot uses TGeant3 class, that is a C++ interface to Geant3[1]. In order to use these class methods is needs the TVirtualMC object must be initialized.

For each subdetector a specific class has been developed which contains the methods to define the materials, the mediums and the volumes. The main methods are:

- CreateMaterials : generates the materials used to build the detector;
- CreateGeometry : builds the detector volumes;
- BuildGeometry : builds the ROOT TNode geometry for the event display;

The detector description, implemented in the *detector.cxx* class, has been quite parametrized in terms of a minimum set of primary members, as a consequence, it is possible to update the geometry by modifying of the same external parameters held in a specific class called MegXXXParam class (the string XXX is the detector name, for MEG experiment it can be equal to LXE, TOF, and DCH), which is loaded in the geometry initialization phase.

4.2.4 Simulation output

Without discussing in details the simulation step, illustrating the particle transport and the detector response, we give a brief overview on the output of the simulation step that will be used as input to start the reconstruction.

The MegRoot simulation framework generates data at different stages of the simulation process. First, there are the so–called *hits* that represent the precise information about a particle passing a detector obtained from the transport MC, i.e., in most cases, energy deposition and local position. These hits are then transformed into the signal produced by the detector, *summable digits* that correspond to the raw data before addition of noise and threshold subtraction. The introduction of summable digits is necessary in order to merge an underlying signal free event with a signal event. The digitization step, them produces *digits*, which have exactly the raw data format, starting from a sample of summable digits, possibly coming from

[1] each Geant3 subroutine is a method for TGeant3 class

the simulation of several events piled–up in the detector integration time window.

In order to run a simulation job the user must initialize a MegSimulation object and apply the method Run(), with argument equal the number of the events to be processed.

The MegRoot modularity allows to run independently the three simulation steps and to produce output corresponding to *hits, sdigits* and *digits.*

4.3 Data simulation in DCH System

The main component of the MEG spectrometer is the Drift CHamber system (DCH). It consists of a set of drift chambers which measure the position of a charged particle along its trajectory.

In the MEG drift chambers it is possible to determine the coordinates of the point of closest approach of the track to the anodic wire from

1. *Measurements of the drift time.*

2. *Measurements of the pulse–height ratios on pick–up electrodes (pads or strips).*

The first measurement, known the drift velocity of the ionization electrons along their drift trajectory, provides the distance between the sense wire and the projection of the point of closest approach in the plane perpendicular to the wires. The second one allows to determine the coordinate of the track along the sense wire direction [59].

A brief description of the procedure used to simulate these measurements in MegRoot is done here.

An electric signal is generated for each read–out channel sensing the ionizing particle track with amplitude and shape defined according to the characteristic of the MEG front–end electronic chip.

Afterwords this is digitized and stored in the raw data block with a format defined by the MEG read–out system and described in §4.3.4.

4.3.1 Simulation of the timing measurement

When a charged particle crosses a sensitive gas volume, it ionizes the gas, thus producing free electrons and positive ions. The electrons, under the effect of the electric field, drift toward the anodic sense wire. At short

distance from the anode the strong electric field allows the development of a charge avalanche from an exponential multiplication process due to the collisions of the electrons with the gas atoms. In proportional regime the electric signal of amplitude correlated to the amounts of charge in the avalanche is produced. The timing of such signal is, instead, related to the time necessary for the ionization charge to reach the sense wire (drift time).

However, the time measurement associated to each hit in the MEG drift chambers system is not directly equal to the drift time, but it can be well described by the relation

$$t_{measured} = t_{drift} + t_{propagation} + t_{flight} + t_0 + \Delta t \tag{4.1}$$

where the $t_{measured}$ is the real data stored in the spectrometer buffer and represent the time delay between the trigger signal (starting time) and when the signal, generated on the sense wire, is read out from the front–end electronics. The terms that are contributing to the $t_{measured}$ in (4.1) are:

- t_{drift} :
  the drift time, that is the time elapsed between the primary ionization and when the charge is collected on the sense wire;

- $t_{propagation}$:
  the time necessary for the propagation of the electric signal along the wire from the location of the energy deposition originating the signal to the front–end electronics;

- t_{flight} :
  the time of flight of the charged particle from the muon decay vertex in the target to the entrance of the drift cell;

- t_0 :
  a common offset due to details of the instrumental apparatus[2]

- Δt :
  the relative delay (which can be positive or negative) of the event generating the current track with respect to the event generating the trigger which activated the data acquisition.

[2] The t_0 can be determined, for example, by special runs at low beam intensity, recording radiative Michel decay. In MegRoot an arbitrary value of 20 ns has been assumed for this variable.

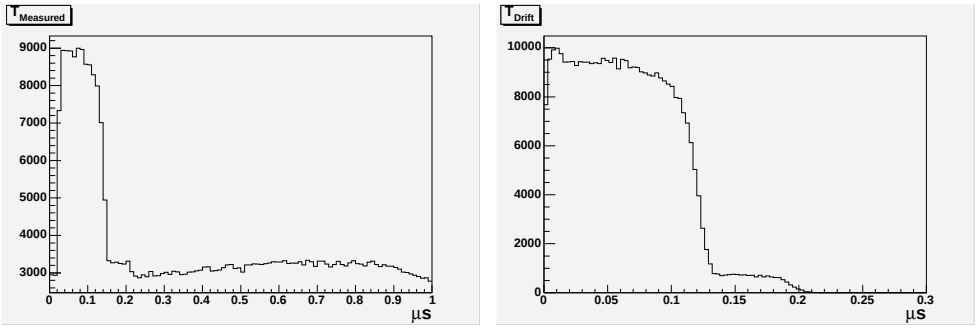

(a) (b)

Figure 4.5: a) *Time distribution in the spectrometer;* b) *drift time distribution.*

Two of these terms, the $t_{propagation}$ and t_0, can be evaluated and subtracted by a suitable data calibration procedure, during the data analysis; t_{flight} can be neglected, its value being of the order of one ns for the first turn of the track in the MEG spectrometer, while Δt is characterizing the timing measurement. As it is shown in fig.4.5 the $t_{measured}$ spectrum extends over the whole dynamic range allowed for the time measurement (in the simulation the acquisition time window is set 1 μs), and it consists of a typical drift time spectrum due the tracks related to the trigger, those which have $\Delta t = 0$, superimposed to a continuous drift time spectrum coming from the uncorrelated tracks.

4.3.2 The simulation of the drift time

The free charge generated in the ionization process, drifting under the influence of the electric field, reduces the electric energy in the gas volume by the amount proportional to the potential difference between the sense wire and the point where there was the ionization process. This change in energy is the source of the signal on the sense wire.

The energy difference ($\Delta\epsilon$), as a function of time, can be obtained using the Wilkinson procedure [56]:

$$\Delta\epsilon = qVF(t) \tag{4.2}$$

where the q is a elementary charge, V is the potential and $F(t)$ is a function that rises from 0 and 1 depending on the cell dimensions and on the ion

drift velocity.

Since, the ionization process is stochastic in nature, depending on the gas mixture parameters and the gas volume width, the signal generated on the wire (waveform), is the sum of more signals (everyone due a single ionization process) distributed along the acquisition time window.

In principle, one should be able to distinguish each ionization process that has contributed to generate the waveform, but this would pose some constrains on the electronics front–end as well as on the software development for the reconstruction and analysis of the data.

In MegRoot the hits simulation is based on the mean free path of the charged particle, by the TVirtualMC classes, while the waveform generation is developed in the classes for the *Summable Digits* and *Digits* management.

However, a good approximation independently on the gas mixture and cell configuration, also implemented in MegRoot, is to suppose that only a hit (a single ionization process) is generated in each gas volume, and to consider the closest approach distance to define the hit position. In this way, the entering and the exiting points for each drift cell are temporary recorded, and a linear approximation of the local particle trajectory with a straight line is made. The distance between this straight line and the sense wire defines the distance of drift, that, is converted in a time measurement using the space–time relation.

Generally, this is not a simple relation linear dependence of the time from the distance. Nevertheless, well consolidated calibration procedures allow to obtain it with a good level of accuracy.

At the moment in MegRoot a linear space time relation, corresponding to a constant drift velocity of 4 $cm/\mu s$, is assumed. Any possible anisotropy deriving from the track incidence angle or from magnetic field effects is neglected (see fig.4.5).

The procedure described above, has been developed by the offline group in the MegDCHv1 detector class, where a re–definition of the Stepping method, used by the particle transport system, is made.

4.3.3 Measurement of the pulse–height ratios

The measurement of the coordinate of the track position along the wire direction is made by using the pulse–height recorded on adjacent cathode strips.

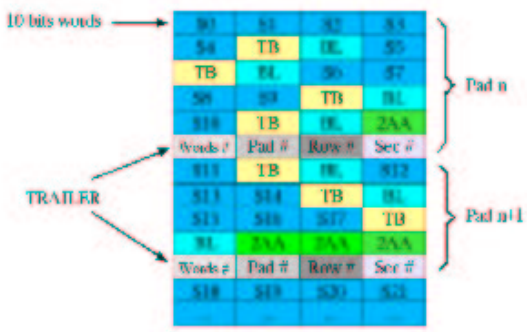

Figure 4.6: *Example of the Raw Data format as inherited from AliRoot.*

The pulse–height ratios is calculated starting from the *pad response function* [59], obtained by integrating the charge density, induced in the cathodic plane, over the area of the strip.

The pad response function depends on the width of the strip (it is important to choose the strip width in relation to the cathode–anode distance, so that the signal ratio on neighboring strips does not make excessive constrains on the dynamic range of the electronics), but also on the gas mixture parameters and on the incidence angle of the track, that implies a spread of the avalanche along the longitudinal coordinate.

At the moment, the pad response function simulation has not been developed in MegRoot, thus the z–coordinate of the cluster position is set equal to the true value, as it comes out from Monte Carlo simulation, smeared with a Gaussian resolution function with σ equal to the expected resolution of the experimental measured (300 μm).

4.3.4 Raw Data Format

The raw data format for the DCH module supported by MegRoot is directly inherited from the AliRoot framework, in particular we are using the raw data general structure developed for the ALICE–TPC subdetector [60].

The basic pulse detection scheme is a fixed threshold scheme: signal of amplitude smaller than a constant level are considered as noise and are rejected. This allows to apply a sample zero suppression algorithm by keeping all the relevant information in the signal sampled over the whole time window.

If one calls *bunch* a group of consecutive bins with signal over threshold coming from one DCH channel, the whole waveform can be represented by

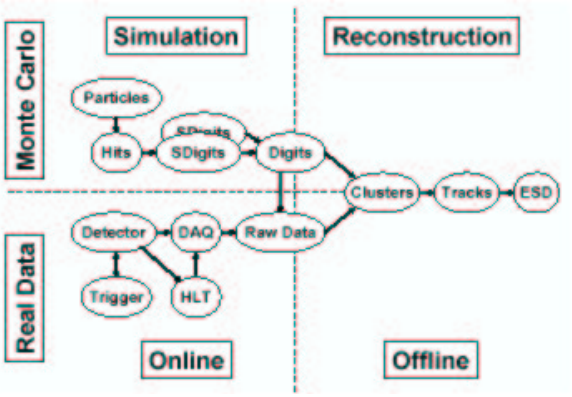

Figure 4.7: *Interaction of the reconstruction code with the other parts of MegRoot.*

a sequence of bunched by recording, for each bunch, n 10–bits words each representing the amplitude of the bin (S_i), the time of the last bin (TB) and the number of bins (BL) respectively, as shown in fig.4.6.

The raw data is composed of a sequence of variable size blocks, each corresponding to a single read–out channel. The block is completed adding a trailer block containing the information about the channel identification (sector, cell or strip number) and the block size, i.e. the number of words in the block.

A dedicated class to menage the decoding and encoding of the raw data has been implemented in MegRoot.

4.4 Reconstruction in MegRoot

The MegRoot reconstruction code is part of the framework. Its modular design, inherited from the AliRoot offline system, allows to compile into separate shared libraries and executed independently any reconstruction task. The reconstruction can use as input both digits in a special ROOT format, more convenient for development and debugging purposes, and digits in the form of raw data, as they are output from the real detector or can be generated from the simulation. The reconstruction outline is shown in fig.4.7: the output of the reconstruction is the Event Summary Data (ESD) containing the reconstructed charged particle tracks, together with the particle identification information, and the particle reconstructed in the calorimeter.

The main steering reconstruction class is MegReconstruction that pro-

vides a simple user interface to the reconstruction. It allows users to configure the reconstruction procedure, include or exclude from the run a detector, and define a suitable sequence of reconstruction steps by enforcing the natural order of the procedures. The full reconstruction can be subdivided into

- local reconstruction: perform the reconstruction for each detector separately;
- vertex reconstruction;
- track reconstruction and particle identification (PID).

The MegReconstruction class is also responsible for the interaction with the MegRoot I/O sub–system and it handles the main loop over the events.

The interface from the steering class MegReconstruction to the detector specific reconstruction code, for the local reconstruction step, is defined by the base class MegReconstructor. For each detector there is a derived reconstructor class that is responsible for creating the corresponding specific *clusters, tracks* and *vertex* finder objects and for passing the corresponding pointers to the MegReconstruction. This allows one to configure the actual reconstruction process using different versions of the reconstruction classes at the detector level.

The local reconstruction step is completed with the *RecPoints* file production, while the whole procedure is completed matching the data from all detectors and generating the ESD file which contains the information on the reconstructed event.

4.4.1 The Reconstruction in the DCH System

The offline track reconstruction strategy adopted for the DCH is based on the Kalman filter approach [57]. Before applying the fit a specific pattern recognition procedure is run in order to define track candidates, solve the left–right ambiguity, and provide a first estimate of the track parameters for the fit. The cluster–finding and the Kalman filter steps are described with more details in the next chapters.

After the reconstruction in DCH the track is extrapolated to the TOF and propagated back to the target in order to find the vertex position, and to calculate the track parameters and their covariance matrix at this point.

The local reconstruction data are stored in the *Track* file, which can be used from user for a partial reconstruction analysis.

The main class is the MegDCHRecoPattern, that through the method MakeClusters() starts the cluster finding loop, while the main class for the Kalman filter is MegDCHtracker.

4.4.2 The Reconstruction in the LXe

In MegRoot, the module describing the Liquid–Xe calorimeter is the LXE module.

As discussed in §3.4, the photons, hitting the calorimeter medium, produce UV scintillation light, that is collect by the photomultipiers (PMT) placed on the calorimeter walls. The measurements of energy, time and direction of the incident particle are provided by the PMT waveform analysis. The reconstruction task is own to give these information starting from the detector data.

Also in the LXE module the main reconstruction steps are the *Clusterization* and the *Track Reconstruction*. The first step allow to group the cells (PMT) where signals were recorded into clusters, while the second step extracts the photon energy and direction.

The whole reconstruction is implemented in the MegLXEClusterizer class [58].

4.4.3 The Reconstruction in the TOF

At the moment the strategy for the local reconstruction in the timing counter (TOF module in MegRoot) has not been completely developed in the collaboration. However, whatever the reconstruction strategy that the collaboration would use, it will be implemented with a logical structure similar to that of the other subdetectors, to guarantee the good functionality of the framework system.

4.5 A MegRoot Section

To start a MegRoot session, after the compilation ad installation of MegRoot code, it is sufficient to launch the command megroot. This allows to enter in the MegRoot software and initialize automatically the MegRun object, called *gMeg*, used to handle all user defined action. At this point it is possible to

run a macro, that is a C++ file containing the commands that must be executed, by the command line:

.x *macro*.C

or inserting step by step the commands as follows

gMeg -> Init() to initialize the setup for simulation step

gMeg -> Run() to run a set of events.

Each user action performed in MegRoot requires a setup initialization defined in the file Config.C. This file is a macro that is automatically executed when the Init() method is called and contains information on:

- the number of events to be processed;
- the geometry configuration to be used;
- the field map.

Moreover, if we use the MegRoot to simulate the events it contains:

- the generation random seeds;
- the event generator used;
- the list of physics processes to be simulated while propagating the particles through the detector.

Chapter 5

The Track Finding Strategy

In the experiments where the detector occupancy is very high the probability that tracks from uncorrelated background events are superimposed to the signal tracks, within the integration time window, is very high. Therefore, in each event recorded, the hits correlated to the trigger signal are merged with hits with a different and random absolute delay with respect to the trigger.

The task of distinguishing the hits belonging to a given track, rejecting noise and uncorrelated hits, is the track finding procedure that makes a track reconstruction in the hit space, also providing a rough estimate of the kinetic parameters of the charged particle, that will be used as the starting point for the track fitting procedure.

In this chapter the strategy for the track finding procedure in the DCH System for MEG experiment as implemented in the MegRoot framework is described. In particular, the basic concept together with the main features of the tracks observed in the MEG spectrometer are discussed. Again, some results on the algorithm performances are shown, when a sample of events data simulated by an external MonteCarlo code (the Pisa MC code) is used. Moreover, the procedure to obtain a first determination of the track kinetic parameters is discussed.

5.1 Data Preparation

In order to allow to run the reconstruction using different input data files, depending on the development level of the code, the class (MegDCHClusterer) has been implemented to manage the different possible input format for the

track finding procedure.

Independently on the data format in input, it can use *hits* from tracking, or *digits* from simulation, or *raw data*, or external data, a MegDCHClusterer object is created for each record in the input file.

By calling to the class constructor it is possible define the *cluster* object as follows:

```
cluster = new MegDCHClusterer(idx,sect,cell,time,zlon);
```

where:

idx is a flag specifying the found of input data relative to the number record (hit, digit or raw data block);

sect is the number of the sector;

cell is the number of the cell;

time is the time measured as defined in §4.3.1 after the calibration step;

zlon is the track position along the wire direction; it comes directly from the pulse–height ratios on the cathodic pads (see §4.3.3).

Afterwords, the cluster is stored in a TObjArray object, named *fBankData*, that is used by the track finding step. In this way a correspondence between the records for a given event and the entries in the *fBankData* is created.

The procedure is run by calling the ReadTree method of the MegDCHRecoPattern class, which loops on the event records creating the cluster object and loading them in the *fBankData*.

5.2 The Track Finder Structure

The task of the track finding procedure is to group hits into disjoint sets representing track segment candidates, taking into account that some hits may be noise or may belong to uncorrelated tracks and, therefore, they must be rejected. Moreover, for each set, the procedure must able to make both a conversion from hit objects into a space points, and to evaluate the initial kinetic parameters of the charged particle associated to the track candidates.

The key concept used to group the hits is a definition of *closeness* in the hit object space. Therefore some parameters, that allow to define a distance between two hits are introduced.

The base class for track finding procedure is MegDCHRecoPattern whose the main methods are MakeClusters, CreateSequence and TrackParameter. The procedure is completed by storing the reconstructed track candidates in the *DCH.RecPoints.root* file, by calling the FillTree class method.

To start the track finding the MegDCHRecoPattern object (*finder*) needs to be initialized by calling the class constructor, when the local reconstruction in the DCH module in MegRoot is called.

5.2.1 The method ReadTree

By calling the ReadTree method the *finder* loads the event data in the format of MegDCHClusterer objects, as produced in the data preparation step. By default the reconstruction would be performed on the simulation output (digits), however other different type input data can be used specifying the TTree object type this flexibility of the framework allows to use a generic input format, thus avoiding dependencies of the algorithms on the specific input data.

After the data load, the ReadTree perform a redefinition of the *fBankData* object requiring that the entries are ordered according to $|zlon|$.

5.2.2 The method MakeClusters

This method performs a selection between the object stored in the *fBankData*, by creating a sequence of MegDCHClusterer objects (clusters) that represents a possible track segment. The method is able to group all objects in the input array into one or more sequence, and to reject the hits that are not associated to any track candidate.

As anticipated, the central concept is the hit closeness: two MegDCHClusterer objects are close in the cluster space if they are topologically close, that is they belong to adjacent cells, and if the time measurements satisfy some requirements. In particular three variables, T_{diff} $T_{average}$ and Z_{diff} are introduced, which have discrimination power between hits belonging to the signal track and noise or uncorrelated hits. Their use will be discussed in next section.

The operative function that generates the cluster sequence is the method AreNeighbours. This is a method returning a boolean value which is true, if the cluster are close, false otherwise. When the true value is returned, the cluster is removed from the bank data and inserted in the cluster sequence,

which is being built.

Using such closeness criterion, the MakeClusters method performs the data clusterization and stores one or more sets of clusters associated to the track segment in the output banks.

The hits that are not clusterized are considered noise or uncorrelated hits and, thus, they are rejected.

5.2.3 The method CreateSequence

This method analyzes each hit sequence created by the MakeClusters. The method performs two actions on the input sequence:

- *makes the conversion from the hit space to the point space*;
- *ensures the quality of the sequence by checking that all hits belonging to the sequence are compatible with a track segment.*

The first step is equivalent to solve the left–right ambiguity problem for drift chambers, namely it determines the space point where the track has crossed the chamber in the plane perpendicular to the drift direction. Using the drift time measurement it is possible to determine a drift circumference in the x–y plane centered in the sense wire position and tangent to the track, within the resolution of the drift distance measurement. In a locally linear approximation of the track, given two consecutive measurements of the drift time, the track can match one of the four tangent straight lines (everyone represent a solution of the so–called tangent problem and defines a pairs of hits) that can be drawn out of the two drift circles. The coordinates of the tangency point are calculated by the method HitPosition that solves analytically the tangent problem in x–y plane. The z of the hit is assigned according to the direct z measurement of the correspondent cluster.

At this level the *hit* object is created, using the MegDCHHits class constructor; it corresponds to the input *cluster* object with the difference that time measurement along the radial direction is replaced with the space coordinates.

For a simple hit pair there are not criteria to distinguish the best tangent that matches the particle trajectory. Therefore, for a track that crosses n sectors with paired hits in each sector, there will be 4^n independent combinations of local segments.

The task of the second step, thus is to define a criterion to choose among all the allowed combinations the one which is best suited to represent a sequence of hits along a particle trajectory.

The criterion is based on the simple observation that, for a good hit sequence, any three consecutive tangency points must be compatible with a parabola with the convexity oriented toward the target region.

This method is a powerful handle to reject the noise and uncorrelated hits, because, for each hit it compares the position with respect to the positions of both the previous and the following hits, thus deciding whether to take or reject it.

The criterion is applied on the hits sequence calling the method Convessity.

5.2.4 The method TrackParameters

The last method called before to store the reconstructed data in the output file, is the TrackParameters method, that performs both, the calculation of purely geometrical parameters of the track, like bending radius and curvature center, and the estimate of the kinetic parameters associated to the track segment, like flight direction and momentum that are used by the track fitting step, as illustrated in the next chapter.

The geometrical parameters are used to label the hit sequences satisfying the convexity requirement, by their root mean square, while the kinetic parameters characterize the track segments associated to each hit sequences.

In particular, to calculate the bending radius, the particle trajectory in the spectrometer is approximated, in the transverse plane, with a circle. Therefore, it is possible to define the circumference center by the crossing point of two straight lines, each perpendicular to a tangent line defined by two hits. As a matter of fact, if the drift distance were not affected by measurement errors, two tangent straight lines would be sufficient to define exactly the circumference center. However, in real life the center is defined using the mean of the distribution of the crossing points defined for each pair of hits. In the same way, the circumference radius is defined as the average on the distances between the center and hit points. In summary each of the 2^n combinations of tangents is associated to a distribution of x_{center}, x_{center} and R. The best combination is assumed to be the one with the minimal spread (RMS) of such distributions.

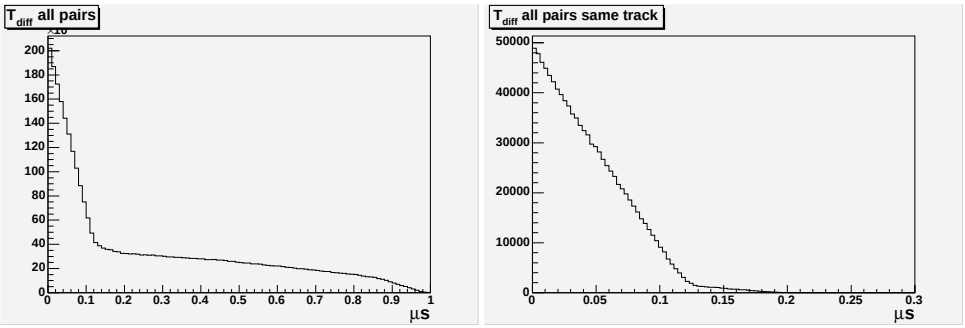

(a) (b)

Figure 5.1: a) T_{diff} *as defined in §5.3.1 for all pairs of hits in adjacent drift cells*; b) T_{diff} *for hits belonging to the same track*

For the best combination, the kinetic parameters are estimated using a approximate linear correlation observed between geometric parameters and track parameters, that will be described in §5.4.

By calling the internal functions Momentum and Angle the momentum and flight direction are returned, while calling the methods SetMomentum and SetAngle the parameter values are saved in the output file.

5.3 Signal Sensitive Parameters

As discussed in §5.2.2, in order to establish the cluster object closeness, three variables, T_{diff}, $T_{average}$ and Z_{diff} are introduced.

Their discriminating power against noise and uncorrelated hits is widely discussed in [61], where a study performed on the Michel positron tracks, that represent the main uncorrelated track source, has been presented.

In the following the main results of this study are shown.

5.3.1 Time Difference

The time difference parameter (T_{diff}) is defined as $t_1 - t_2$, where t_1 and t_2 are the measured times associated to hits in adjacent drift cells. Figure 5.1 shows the T_{diff} distributions in the general case where hits belonging to different tracks can be paired (left) and for hit pairs belonging to a single track. This parameter cannot distinguish the signal track from background tracks; on the other hand, it is helpful in reducing the combinatorial eventually arising

from the confusion of hits belonging to different tracks topologically close in the spectrometer.

Thanks to the sense wire staggering, T_{diff} is related to the position of the track with respect to the closest sense wires in the two cells. Therefore, it can range from 0, if the track is equally distant from the two sense wires, to approximately 150 μs, the maximum drift time, if the track hits ones sense wire and, therefore, is located at the maximum possible drift distance from the sense wire on the other cell. If the hits in the pair do not belong to the same track, T_{diff} can be as large as 1 μs.

5.3.2 Time Average

The $T_{average}$ parameter is defined as the average between the time measurements associated to a pair of hits in adjacent chamber units, after the calibration step. From purely geometrical arguments, for the track related to the trigger $T_{average}$ must be equal to one half of the maximum drift distance in the cell, when the track is following approximately the tangential direction. For tracks out of time, one has in addition the total time offset of the track with respect to the trigger. In fig.5.2 the top–left plot shows the distribution of $T_{average}$ for all possible pairs built out of hits belonging to the same sector. In the right–top plot pairs where both hits belong to the same track are selected. If the requirement that both hits in the pair belong to the trigger related track is added, the long tail of the distribution is cut away. This variable, therefore, is sensitive to tracks in time with the trigger or coming from accidental background. The peak associated to trigger tracks is located at about 65 ns, which correspond to one half of the average drift path:

$$d/2 = 0.065\ \mu s \times 4\ cm/\mu s = 2.6mm \tag{5.1}$$

The plot shows that $T_{average}$ keeps the same shape when calculated for hit pairs belonging to adjacent modules, even if located in adjacent sectors. In spite of the various simplifying assumptions adopted in the simulation, the width of the distribution of $T_{average}$, $\sigma \sim 27$ ns, appears much worse than the limiting figure of 5 ns claimed in the proposal of the experiment. Therefore, a better resolution is obtained when concentrating on the pair in the central sector in the track first turn, if the number of sector is odd, where the trajectory is almost orthogonal to the chamber axis.

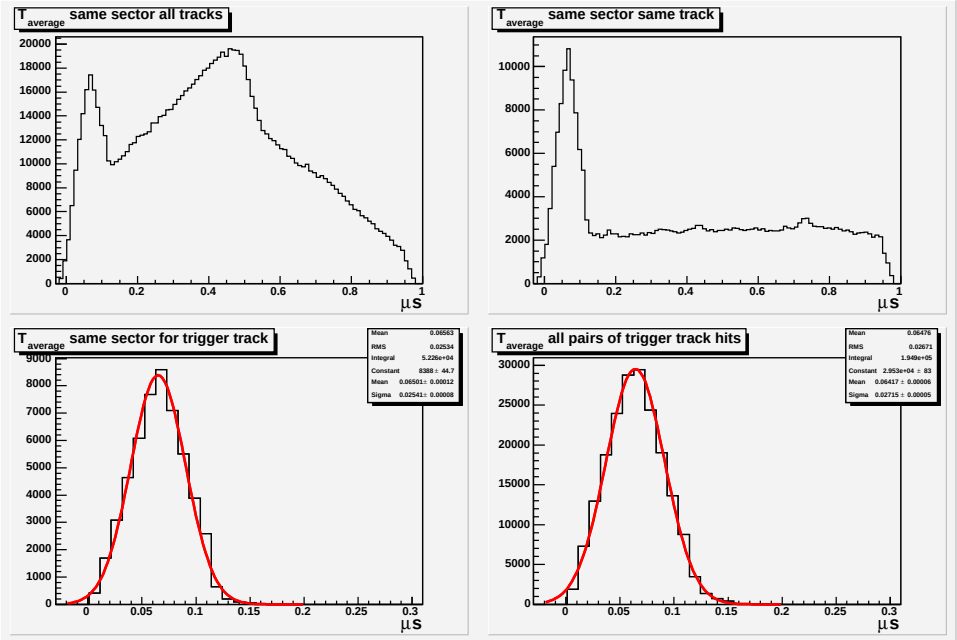

Figure 5.2: left-top: $T_{average}$ *for all pairs of hits in adjacent modules of the same drift chamber.* right-top: $T_{average}$ *for all pairs of hits in adjacent modules of the same drift chamber belonging to the same track.* left-bottom: $T_{average}$ *for all pairs of hits in adjacent modules of the same drift chamber belonging to the track in time with the trigger.* right-bottom: $T_{average}$ *for pair of hits in any adjacent modules belonging to the track in time with the trigger.*

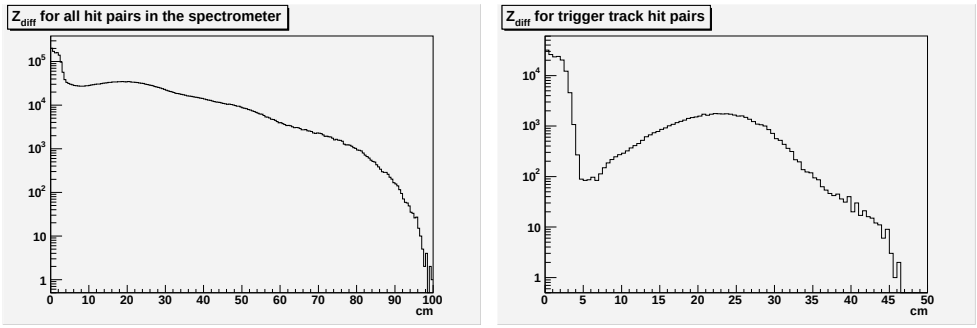

(a) (b)

Figure 5.3: a) Z_{diff} *all hits in the spectrometer*; b) Z_{diff} *event trigger hits.*

5.3.3 The distance along the z–axis

The position of the hits along the longitudinal axis, measured by the cathodic strips on the walls of the chambers, allows to introduce another parameter Z_{diff}, that can be used to define a continuity criteria of the track along this direction. The Z_{diff} parameter is defined as the difference between the z–coordinates for a pair of hits in adjacent chamber modules. Also for this parameter, in fig.5.3 we compare the distribution for all the pairs in the spectrometer and that for pairs belonging to the trigger track and, therefore, to a single track. In the single track case, we notice that the narrow peak at low Z_{diff} values, which has a sigma of about 1.2 cm, is followed by a broad secondary peak, clearly related to pairs consisting of hits belonging to different windings of the positron tracks and, as a consequence, well separated in z, with respect to the consecutive hits in the track path whose distance in z is smaller than a few centimeters. In the general case of pairs from signal and background together the situation is confused by a continuous and not uniform background superimposed to the distribution for single tracks. However, also in this case, a large fraction of the pairs with $Z_{diff} < 5$ cm comes from hits belonging to the first turn of a single track.

5.4 The Kinetic Parameters Estimation

As anticipated in the previous sections the estimate of kinetic parameters of the charged particle is performed by the TrackParameters method of the MegDCHRecoPattern class, which uses the approximation of a linear cor-

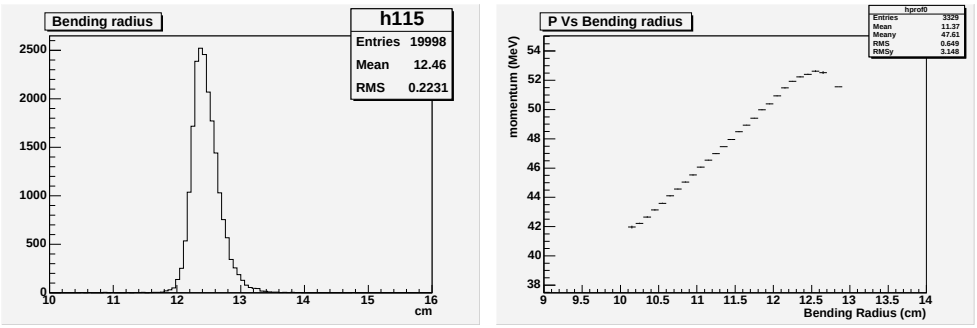

(a) (b)

Figure 5.4: a) *The bending radius distribution for positron tracks from* $\mu \to e\gamma$*;* b) *profile plot of the momentum as a function of the bending radius for Michel positron tracks.*

relation between kinematic parameters and geometrical properties of the reconstructed track segment.

The track parameters, which are essential to the track fitting procedure, are the particle momentum (p), and the particle flight direction defined by the two angles (φ and θ) that the particle trajectory forms with the x and z axis respectively.

In this section we discuss the observed linear correlation existing between the kinematic and geometrical track parameters for both Michel and signal positrons tracks, quoting also the precision of the approximation.

5.4.1 Momentum correlation

As shown in §3.3.1, the main advantage in using the COBRA spectrometer is that the gradient magnetic field is arranged such that monochromatic positrons from the target follow trajectories with a constant projected bending radius independent of the emission angle.

In the approximation where the particle trajectory is a circumference in the transverse plane, we need three points to define it analytically. However, if we suppose to fix the particle starting point (vertex), that is equivalent to suppose that events are generated point like in the reference frame origin, only two points are sufficient to define analytically the particle trajectory.

Fig.5.4.a shows the bending radius distribution for a sample of positron tracks from $\mu \to e\gamma$ decay when the coordinates of the first and last hit, in

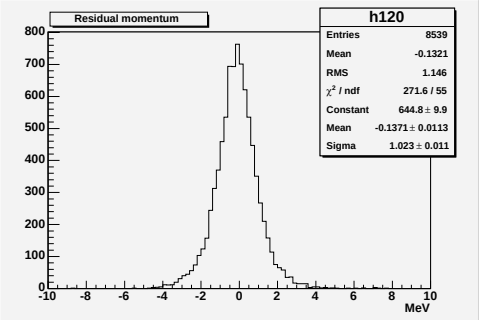

Figure 5.5: *Residual distribution for positrons momentum.*

the track segment, are used to define the circumference. The mean value of:

$$r = (12.5 \pm 0.2)\ cm \tag{5.2}$$

allows to identify the signal tracks in the spectrometer.

Completely different is the case in which the positron tracks from Michel decays are analyzed, since the particle momentum may assume a value in a wide range. However, if we choose to plot the particle momentum as a function of the bending radius of the track, we notice as these parameters are linearly correlated (fig.5.4.b). Comparing the two plots, we note as the value of the bending radius for positron signal tracks is perfectly located at the end point of the bending radius spectra for the Michel positron tracks. In this way, we can define a linear function to calculate the momentum of the particle from the bending radius. A simply relation based on the plot in fig.5.4 is:

$$p = a + b * r \tag{5.3}$$

where p is the positron momentum and r is the trajectory bending radius. The best estimate for the free parameters a and b is

$$a = -8.04 \pm 0.18\ MeV/c$$
$$b = 4.89 \pm 0.02\ MeV/c{\cdot}cm$$

The fig.5.5 shows the distribution after residuals of between the true positron momentum and the reconstructed one where this parametrization is used. The Gaussian fit tells us that the procedure described above is able to provide the charged particle momentum with an error $\Delta p/p = 2\%$.

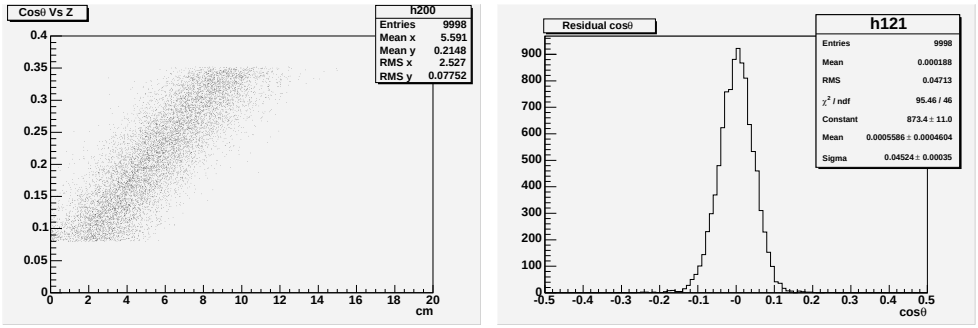

(a) (b)

Figure 5.6: a)*Scatter plot of the* $\cos\theta$ *as a function of the* z*–coordinate for positrons from* 52.8 MeV. b)*Residuals for* $\cos\theta$ *when the parametrization in (5.4) is used.*

5.4.2 $\cos\theta$ correlation

One of the parameters that characterizes the flight direction is the θ–angle, that is the angle that the vector tangent to the particle trajectory in the vertex point forms with the longitudinal axis (z). However, since the detector design imposes that only positron emitted with $0.08 < |\cos\theta| < 0.35$ are observed, we prefer to use the cosine of the θ angle for an easy comparison with the generated values. Moreover, the flight direction is independent from the momentum, therefore samples of positrons from the $\mu \to e\gamma$ or from Michel decays can alternatively be used to study the correlation of $\cos\theta$ from directly measured quantities.

The scatter plot of the $\cos\theta$ as a function of the z–coordinate of the first hit along the particle trajectory (see fig.5.6) shows as these parameters are tied by a linear correlation: the fit gives the following parameter values:

$$offset = 0.03 \quad and \quad slop = 0.03\ cm^{-1} \tag{5.4}$$

Using this parametrization on both positron tracks from signal (Michel) decay we obtain a standard deviation for the residuals of $\sigma_{\cos\theta} = 0.045$ ($\sigma_{\cos\theta} = 0.039$); for a mean value of $\cos\theta$ ($\langle\cos\theta\rangle = 0.26$) the error propagation entails an uncertainty on the θ angle of about 47 $mrad$ (40 $mrad$).

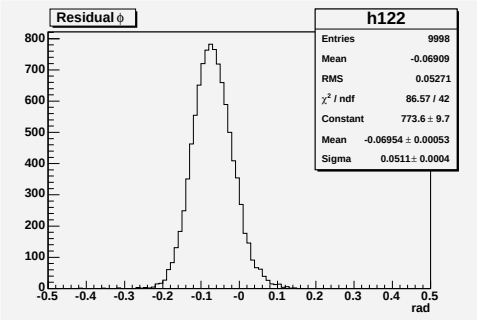

Figure 5.7: *Residual distribution for phi angle.*

5.4.3 φ–angle

The φ–angle, defined as the angle between the x axis and the projection of the flight direction at the vertex on the transverse plane, is the other parameter that defines the track direction along with θ.

In the same approximation used to define the bending radius, i.e. the positron trajectory is a circle in the x–y plane crossing the reference frame origin, the φ–angle is defined by the tangent to the circumference in the vertex point. Since the tangent direction is perpendicular to the circumference radii at each point, we can use the coordinate of the circumference center to define the angle. In particular, we call x_c and y_c the coordinates of the center of the circle the φ–angle is given by:

$$\varphi = \arctan\left(-\frac{x_c}{y_c}\right) \tag{5.5}$$

The residual distribution for this parameter (see fig.5.7) shows as the method used to estimate it introduce a bias: in particular since the residual is defined as

$$Res_\varphi \quad = \quad \varphi^{MC} - \varphi^{rec}$$

the method overestimate the φ–angle of a quantity equivalent to the mean value of the residual distribution. However, we'll see in the next chapter that offset of 70 *mrad* in average does not affect the track fitting performances.

5.5 Results

In this section some results obtained with the track finding procedure outlined above are discussed. In particular the discriminating power of the

sensitive parameters discussed in §5.3 is tested. The cluster finding procedure has been tested using a sample of Michel and signal positron tracks, simulated by an external Monte Carlo code (so–called the Pisa version) and using the applying the cuts listed below:

- difference in z: $Z_{diff} \leq 3.5\ cm$
- time difference: $T_{diff} \leq 0.2\ \mu s$
- time average: $T_{average} \leq 0.2\ \mu s$

moreover we have imposed that the calibrated time for each hit is less than $0.3\ \mu s$ and the sum of the calibrated drift distance for adjacent hit must be less than the distance between the sense wire position within the chamber resolution (within 3σ).

The track segments reconstructed are finally labeled by the kinematic parameters of a positron track they are supposed to represent. Eventually, if in a trigger the track finding procedure will reconstruct one or more pile–up track segments the final fitting step will have rough precision to reject a large fraction of them.

5.5.1 Results with Michel positrons

The first test has been performed on a sample of events where the signal track (in time with the trigger) was superimposed to a number of tracks out of time. The background track multiplicity was defined with a Poisson distribution with mean value equal to five. Both the track correlated to the signal trigger and the uncorrelated tracks are generated with the kinematics of Michel positrons.

Using the value shown above for the signal discriminating parameters, the cluster finding procedure allows to achieve a 94.4% of efficiency on the reconstructed events.

In more detail in 64.9% of the reconstructed events, the procedure has been able to select only the clusters associated, via Monte Carlo identifier, to the track correlated to the signal trigger, rejecting quite the hits belonging to the uncorrelated track.

Moreover, in 12.02% of reconstructed events the procedure also has been able to select a second hit cluster associated to the second turn of the signal track in the spectrometer. In a low fraction of the reconstructed events

(0.27%) more than two segments associated to the signal track have been built.

The full summary on the cluster finding performances is shown in table5.1, where the reconstructed events are grouped by the number of track segment associated to the signal and by their purity. As an example, out of 3995 events where only one sequence associated to the trigger has been found, in 3862 events such track candidate did not include any background hit, 101 track candidates contain 1 background hit and so forth.

The total inefficiency, for reconstructing at least one sequence related to the trigger track, is about 5.6%. However this is overestimated, since, in several cases of failure of the step, the simulated signal track has only four hits, or less, in the first turn and therefore it cannot be really reconstructed.

The last comment concerns the purity level of the reconstructed track

	Nr. of events		fractions	
Nr. of ev.s with 1 trigger seq.	3995	(2703)	77.72%	(52.59%)
100% purity	3862	(2632)	75.14%	(51.21%)
1 hit from bkg.	101	(55)	1.96%	(1.07%)
2 hits from bkg.	22	(12)	0.43%	(0.23%)
>2 hits from bkg.	10	(4)	0.19%	(0.08%)
Nr. of ev.s with 2 trigger seq.s	842	(618)	16.38%	(12.02%)
100% purity	792	(588)	15.41%	(11.44%)
1 hit from bkg.	35	(21)	0.68%	(0.41%)
2 hits from bkg.	8	(6)	0.16%	(0.12%)
>2 hits from bkg.	7	(3)	0.14%	(0.06%)
Nr. of ev.s with >2 trigger seq.s	16	(14)	0.31%	(0.27%)
Nr. of ev.s without trigger seq.s	287		5.58%	
$\geq$ 1 pile–up sequence	124		2.41%	
no sequences	163		3.17%	

Table 5.1: *Result of the Cluster Finding. The signal track is a positron from a Michel decay in time with the trigger. The second and third columns list the number of events for each category. In column fourth and fifth the normalization is performed against the number of events in which the simulated track in time with the trigger has at least five hits (5140 events). The values in brackets refer to events where only sequences associated to the trigger track have been built.*

	Nr. of events		fractions	
Nr. of ev.s with 1 trigger seq.	5884	(4071)	95.04%	(65.76%)
100% purity	5747	(3993)	92.83%	(64.50%)
1 hit from bkg.	101	(58)	1.63%	(0.94%)
2 hits from bkg.	22	(10)	0.36%	(0.16%)
>2 hits from bkg.	14	(10)	0.23%	(0.16%)
Nr. of ev.s with 2 trigger seq.s	257	(173)	4.15%	(2.79%)
100% purity	224	(150)	3.62%	(2.42%)
1 hit from bkg.	21	(16)	0.34%	(0.26%)
2 hits from bkg.	6	(3)	0.10%	(0.05%)
>2 hits from bkg.	6	(4)	0.10%	(0.06%)
Nr. of ev.s with >2 trigger seq.s	-	-	-	-
Nr. of ev.s without trigger seq.s	50		0.81%	
$\geq$ 1 pile–up sequence	25		0.40%	
no sequences	25		0.40%	

Table 5.2: *Cluster Finding statistic over a sample of $\mu \to e\gamma$ events with pile-up. The normalization is performed against the number of events in which the track in time with the trigger has at least five hits. The values in brackets refer to events where only sequences associated to the trigger track have been built.*

segment. From table5.1 about the 97% of the hit clusters associated to the trigger signal do not contain any background hit. Moreover, the remaining sample of impure hit sequences has an average content of background hits equal to 15%.

5.5.2 Results with signal positron

The same procedure has been applied to a sample of simulated $\mu \to e\gamma$ decays; the timing of the corresponding positron tracks is defined assuming that these events are triggering the DAQ. An average number of tracks from simulated Michel decays, corresponding to the expected rate of 5 MHz, is superimposed to the signal event with uniform random time offset with respect to the trigger.

For this sample of signal events the cluster finding performances, as shown in table5.2, are slightly better due to the higher momentum of the

signal tracks (52.8 MeV/c) compared to a wide momentum spectrum of the Michel superimposed tracks ($30 \div 50$ MeV/c), which correspond to longer track paths into the MEG spectrometer.

The inefficiency is less than 1% and the percentage of pure hit clusters is about 98%. On the other hand, the contamination from hit clusters associated to pile–up tracks is basically unchanged: in the 68% of the events only the clusters associated to the trigger track are selected.

Chapter 6

The Track Fitting

After the Track Finding procedure, where the hits recorded in the tracking detector are collected into subsets each of them associated to a track segment, the determination of the track parameters requires a precise track model for the trajectory of the charged particle in a magnetic field, and the knowledge both of the detector resolutions and of the amount of material traversed by the particle in order to have a correct and efficient description of the multiple scattering and energy loss effects.

The accurate reconstruction of the track parameters from a set of space points and the back–propagation to the vertex, with the complete use of the information available from the tracking device, is defined Track Fitting step.

In this way, the track fit can be viewed as the last step in the data reconstruction, which has in input the position of the hits provided by the track finder, whereas its output is a list of particles represented by an estimate of the track parameters.

In this chapter, a track fitting strategy, based on the Kalman filter [57], and implemented in MegRoot for the data reconstruction in the DCH detector is described. In particular, the basic idea, the analytic formulation, the implementation and the performances of the Track Fitting procedure are discussed.

6.1 The Kalman Filter Technique

The Kalman filter technique was developed to determine the evolution of a dynamical system from a set of measurements taken at different times [62].

Essentially, it consists of a set of mathematical equations that provide,

by recursive steps, the description of the system state by minimizing the sum of squared residuals normalized to the errors. Therefore it proceeds by a succession of alternating prediction and decision steps, from one measurement to the next, thus improving the knowledge on the system parameters by following the evolution of the so–called "state vector": a list of features describing the system.

In the prediction step, the current state vector extrapolated to the next measurement conditions is preformed, taking into account all possible effects that affect the system (for example, if the system is a charged particle these effects could be the multiple scattering and energy loss), while in the filter step the state vector is updated taking into account, with the appropriate weight, the present measurement.

After each prediction step, the filter has to decide whether the measurement is compatible with the present vector state extrapolation and, then, if it should be used in the subsequent update of the state vector or if it should be rejected. Conventionally, the measurement which is closest to the prediction is selected for inclusion in the updated state. The distance is expressed by a suitable test variable, for example a χ^2.

6.2 The Track Fitting Strategy

The final purpose of the tack fit is to estimate a set of parameters (state vector) that describes the charged particle using a set of measurements along the track trajectory.

As previously anticipated, the fitting procedure in MegRoot is based on the Kalman filter and, therefore, it inherits its logical structure. The basic idea: every space point added to the track updates its state vector; a space point is added to the track depending on its compatibility with the track extrapolation on the relevant measurement plane.

Obviously, before starting it is necessary to initialize the state vector and the covariance matrix.

6.2.1 The Analytical Formulation of the Track Fit

This section gives a more technical presentation of the idea that was described above.

First of all, it is necessary to define the state vector that allows to de-

scribe the system evolution. Since the system is a charged particle and the time evolution is the particle trajectory, the state vector can be represented by a collection of five parameters: two for the position, two for the direction and one for the track curvature or particle momentum.

If we choose to work in a cylindrical reference frame with the z axis oriented along the detector axis and the radius given by $r = \sqrt{x^2 + y^2}$, the *state vector* may be represented by:

- r, the radius where the trajectory intersects the reference plane at azimuthal angle φ_0;

- z, the z value where the trajectory intersects the reference plane;

- $\varphi_{dir} - \varphi_0$, the phase angle of the helix at the intersection with the reference plane (φ_{dir} is the angle of the tangent to the trajectory at this point);

- $\tan\lambda$, where $\lambda = \arctan p_z/p_\perp$ is the dip angle of the helix.

- $1/p$, the inverse particle momentum;

In the notation used here, the particle state vector at the time k is denoted by $\tilde{x}_k$ and the its covariance matrix by C_k. In our case, $\tilde{x}_k$ is parametrized in terms of the track parameters which are actually defined as $\tilde{x}_0$, i.e. the state vector at the decay vertex. The matrix F_k describes the propagation of the track parameters from the hit $(k-1)$ to the hit k[1]. The space point measured at the kth measurement plane is denoted by m_k (in general, m_k is a vector with the dimension of that specific measurement, i.e. for a tracking device m_k is a space point). The measurement error is described by the matrix V_k; while the relation between the track parameters $\tilde{x}_k$ and the predicted measurement is described by the projection matrix H_k.

In each filter step, the state vector and its covariance matrix are propagated to the location of the next measurement with the prediction equations:

$$\tilde{x}_k^{k-1} = F_k \tilde{x}_{k-1} \tag{6.1}$$

$$C_k^{k-1} = F_k C_{k-1} F_k^T + Q_k \tag{6.2}$$

[1] We assume at this stage a linear system, so that F_k and H_k, defined later on, are matrices in the proper sense.

and the estimated residual r_k^{k-1} with its errors (R_k^{k-1}) become

$$\begin{aligned} r_k^{k-1} &= m_k - H_k \tilde{x}_k^{k-1} && (6.3) \\ R_k^{k-1} &= V_k + H_k C_k^{k-1} H_k^T && (6.4) \end{aligned}$$

Here, Q_k denotes the additional error introduced by any noise source present in the system, i.e. random perturbation of the particle trajectory, for example, multiple scattering.

The update of the system state vector with the kth measurement is performed with the filter equations:

$$\begin{aligned} K_k &= C_k^{k-1} H^T (V_k + H_k C_k^{k-1} H_k^T)^{-1} \\ \tilde{x}_k &= \tilde{x}_k^{k-1} + K_k (m_k - H_k \tilde{x}_k^{k-1}) \\ C_k &= (1 - K_k H_k) C_k^{k-1} \end{aligned} \qquad (6.5)$$

where the K_k matrix is called the gain matrix.

The χ^2 contribution of the filtered point is then given by

$$\chi_k^2 = r_k^T R_k^{-1} r_k \qquad (6.6)$$

The system state vector at the last filtered point always incorporates the full information from all previously accepted measurements.

6.2.2 The Multiple Scattering

Multiple Scattering occurs through the elastic scattering of charged particles in the Coulomb field of the nuclei in the detector materials. Since the nuclei are usually much heavier than the traversing particles, the absolute momentum of the latter remains unaffected, while the direction is changed.

The stochastic nature of multiple scattering is well described by the Molière theory [63]. However, for many applications it is sufficient to use the so–called *"average scattering angle*, defined by the projected angular distribution of scattering angles as [64]

$$\theta_0 = \frac{13.6\ MeV}{\beta c p} z \sqrt{\frac{x}{X_0}} \left[1 + 0.038 \ln \frac{x}{X_0} \right] \qquad (6.7)$$

where p, βc and z are the momentum, velocity and the charge (unsigned and normalized to the e^- charge) of the incident particle, while the x/X_0 is the thickness of the scattering medium in terms of radiation lengths.

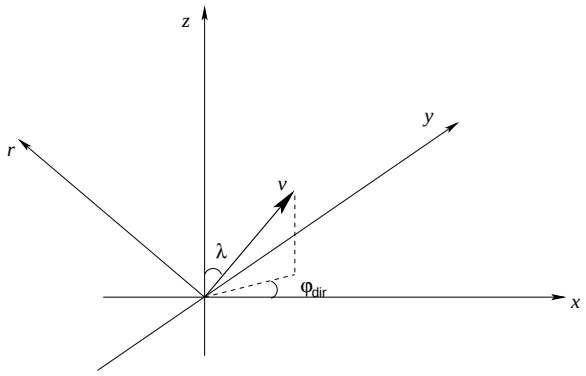

Figure 6.1: *Geometry for the Multiple Scattering.*

In general, multiple scattering could be treated in the track fit by expressing the angular uncertainty introduced by each thin scatterer as an additional contribution to the error on the track extrapolation at the relevant measurement plane. Since a track deflection by Coulomb scattering will influence all measurement errors along the particle trajectory in a correlated way, this would imply that the matrix V in §6.2.1, that describes the measurement errors, would become not diagonal.

In order to avoid this complication, in the Kalman Filter procedure, multiple scattering effects are taken into account by a suitable matrix (Q_k) in the transport equations (6.1). This matrix is defined as

$$Q_k = \theta_0 \cdot A_k \tag{6.8}$$

where the θ_0 is the average scattering angle at the location of the kth hit, while A_k is a symmetric 5×5 matrix that expresses the artificial correlation between the state vector parameters due to the multiple scattering effects.

Fig.6.1 shows the geometry involved to describe the Multiple Scattering effects on the track parameters: $\vec{V}$ is the vector tangent to the particle trajectory, $\vec{r}$ is the vector perpendicular to the track and pointing toward the center of curvature, the two angles φ_{dir} and λ define the particle direction. The multiple scattering is described by two uncorrelated scatterings in two perpendicular planes that contains the vector V, as described in [65]: the first plane is the plane spanned by the vector V and $\hat{z}$, while the second one is the plane perpendicular to the vector r. Each scattering angle is an average described by the parametrization in (6.7)

Using the parametrization in §6.2.1 for the state vector the matrix A_k

can be written like

$$\begin{pmatrix} \frac{L^2}{3}\frac{1}{\cos^2\alpha} & \frac{L^2}{3}\frac{1}{|\cos\alpha|}\tan\alpha\tan\theta & \frac{L}{2}\frac{\sqrt{\eta}}{|\cos\alpha|} & 0 & 0 \\ \frac{L^2}{3}\frac{1}{|\cos\alpha|}\tan\alpha\tan\theta & \frac{L^2}{3}\left(\eta+\tan^2\alpha\tan^2\theta\right) & \frac{L}{2}\sqrt{\eta}\tan\alpha\tan\theta & \frac{L}{2}\eta\sqrt{\eta} & 0 \\ \frac{L}{2}\frac{\sqrt{\eta}}{|\cos\alpha|} & \frac{L}{2}\sqrt{\eta}\tan\alpha\tan\theta & \eta & 0 & 0 \\ 0 & \frac{L}{2}\eta\sqrt{\eta} & 0 & \eta^2 & 0 \\ 0 & 0 & 0 & 0 & 0 \end{pmatrix} \tag{6.9}$$

where

- L is the track length at the kth plane measurement
- α is defined as $\frac{\pi}{2} - (\varphi_{dir} - \varphi_0)$
- η is the derivative of the $\tan\lambda$ with respect to λ

The diagonal elements represent the correction to the state vector parameters due to the multiple scattering effects; in particular we note as the last term in (6.9) is null because the multiple scattering does not affect the positron momentum.

6.2.3 The Energy Loss

At low energies positrons lose their energy mainly by ionization, although other processes, like Bhabba scattering, e^+ annihilation or bremsstrahlung can occur. Therefore, energy loss effects as an function of the mass width can be described using the Bethe–Block formula:

$$-\frac{dE}{dx} = Kz^2\frac{Z}{A}\frac{1}{\beta^2}\left[\frac{1}{2}\ln\frac{2m_ec^2\beta^2\gamma^2T_{max}}{I^2} - \beta^2 - \frac{\delta}{2}\right] \tag{6.10}$$

where $K = 0.307075\ MeVg^{-1}cm^2$, and T_{max} is the maximum kinetic energy which can be transfered to a free electron in a single collision.

The value of the other parameters in (6.10) for the medium traversed by the particle along its trajectory are reported in table 6.2.3

The energy loss by bremsstrahlung is also taken in to account in the current implementation of the Kalman filter procedure although it does not contribute in a relevant way of the positron energies involved.

6.3 The Track Fitter Structure

The procedure described above is implemented in two classes in MegRoot, MegDCHtracker and MegDCHtrack.

material	Z/A ($g^{-1}mol$)	density (gcm^{-3})	Mean excitation energy (eV)	Radiation length (cm)
helium	0.49968	0.1786E-03	41.8	756
ethane	0.59861	1.356E-03	45.4	34035
kapton	0.51264	1.42	79.6	28.6
nitrogen	0.49976	1.25E-03	82.0	47.1

Table 6.1: *Atomic and physics properties of some materials used in the MEG spectrometer. The value are the same reported in the PDG.*

The first class is the base class for the Track Fitter in the DCH module and it drives the full fitting procedure, starting from data loading to the production of the final result. The second class handles the mathematical aspects of the track fit: the Runge–Kutta method for the particle transport, the calculation of the multiple scattering effect and the energy loss, determination of the covariance matrix.

Essentially, the track fitting procedure follows the steps implemented in the main methods of the MegDCHtracker class:

LoadClusters
it load the data in input and prepare them for the fit (i.e. sequences of hits collected as track candidates by the pattern recognition).

MakeSeeds
it initializes the state vector and covariance matrix used by the track fitter. The state vector is initialized using the coordinates of the first point in the subset and the track parameters (momentum and flight direction) as estimated in the track finding step, while the covariance matrix is initialized with arbitrary values.

Clusters2Tracks
it performs the conversion from the subset (cluster) of space points to the track segment by the track propagation from the first point to the last point in the subset.

RefitTrack
it represents the track fitter core: the method performs the calls to the MegDCHtrack class methods which allow to perform the fitting procedure as described in the previous section.

6.4 The Track Fitter Results

As discussed in §5.4 the parameters that allows to parametrize a particle track in the MEG Spectrometer are its momentum and its flight direction, defined by the φ and θ angles, in the vertex point, together with the space coordinate of the vertex.

Since the state vector of the track is defined as shown in §6.2.1, the fit don't provide directly the required track parameters but it is necessary to derive they from the state vector definition. In particular, by calling state[i] (with $i = 1, ...5$) the ith component of the state vector propagated to the origin, from its definition it follows:

$$\begin{aligned}
p &= \frac{1}{state[5]} & \sigma_p &= \left| -\frac{1}{(state[5])^2} \right| \sqrt{C_{5,5}} \\
\theta &= \arctan(state[4]) & \sigma_\theta &= \left| -\frac{1}{1+(state[4])^2} \right| \sqrt{C_{4,4}} \\
\varphi &= state[3] + \varphi_0 & \sigma_\varphi &= \sqrt{C_{3,3}} \\
r_0 &= state[1] & \sigma_{r_0} &= \sqrt{C_{1,1}} \\
z_0 &= state[2] & \sigma_{z_0} &= \sqrt{C_{2,2}}
\end{aligned} \tag{6.11}$$

where p, θ and φ are the initial kinematic parameters of the particle while r_0 and z_0 are the radial and longitudinal coordinates of the vertex in the reference plane ($z = 0$).

The results presented here concern a preliminary test performed on a sample of 7000 positron tracks from $\mu \to e\gamma$ decay. We have used a track sample generated from point like vertex, in order to easily check the fit performances for vertex reconstruction; moreover the track generation follows the usual angle distributions ($-60° < \varphi < 60°$ and $0.08 \leq |\cos\theta| \leq 0.35$) according to the detector geometrical acceptance.

6.4.1 The kinematic parameters

As discussed in §5.4 the track finding procedure provides a first estimate of the positron momentum with a precision of about 2%. This value is not sufficient to achieve the experiment sensitivity for the $\mu \to e\gamma$ search, as declared in the experiment proposal where positron momentum resolution of 0.7%–0.9% in FWHM is required.

The momentum distribution for positron track reconstructed after the fitting procedure is shown in fig.6.2. This plot refers to a sample of simulated

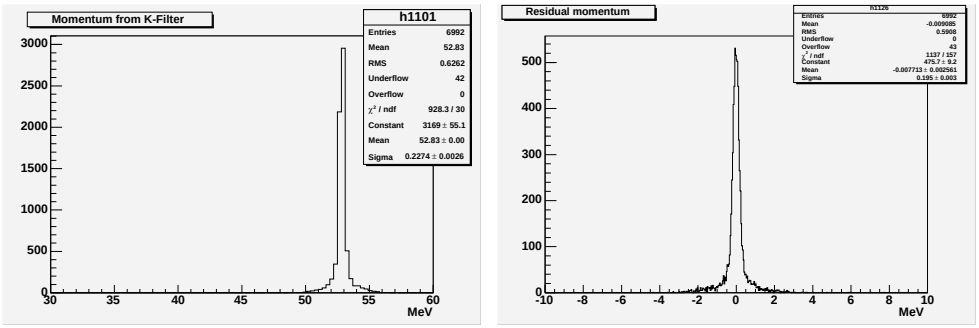

(a) (b)

Figure 6.2: *The momentum distribution (a) and residuals (b) for positron tracks after the fitting procedure.*

positrons from the $\mu \to e\gamma$ decay. The mean value of the distribution is 52.8 MeV in perfect agreement with the generation value.

However, if we consider the residual plot fig.6.2(right) where the

$$\Delta p = p^{true} - p^{rec}$$

is plotted, we note as the fit gives an overestimate on the momentum of about 8 keV, while the relative error is $\Delta p/p = 0.4\%$ corresponding to 0.9% FWHM.

Note as the fitting procedure allows to bring down of a factor 5 the momentum resolution, with respect to the corresponding resolution provided by the pattern recognition; however, new refinements of the fitting procedure are necessary in order to eliminate the not Gaussian tails in the momentum distribution in fig.6.2 (about 7% of events are out of the 3σ range), thus improving the overall resolution and also to correct for the bias on the average.

Concerning the flight direction the fit allows to improve the parameter resolutions with respect to the first estimate given by the pattern recognition. In particular, considering the parameter residuals show in fig.6.3 we obtain a $\sigma_\varphi \simeq 3\ mrad$ and a $\sigma_{\cos\theta} \simeq 0.003$ that correspond to $\sigma_\theta \simeq 3\ mrad$ representing an improvement of a factor 10 with respect to the resolutions quoted in the track finding.

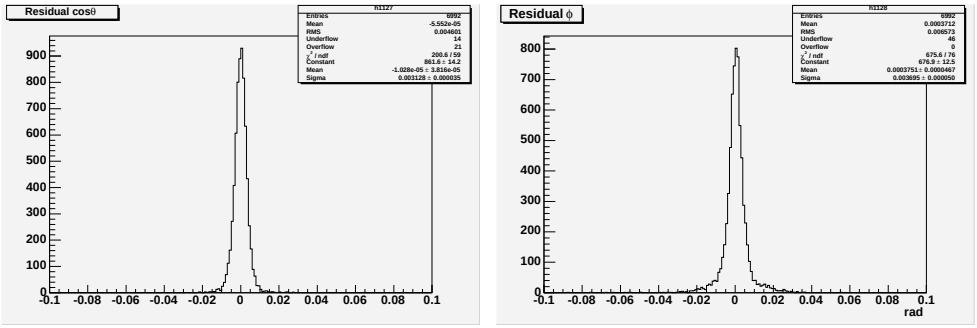

(a) (b)

Figure 6.3: *The residuals on* $\cos\theta$ *(a) and* φ *(b) parameters from the fitting step.*

6.4.2 The vertex calculation

In the parametrization described in §6.2.1 of the state vector it is possible to estimate the track vertex using the first and second coordinate: in particular the first give the radial distance from the origin of the vertex in the transverse reference plane (x–y plane), the second one the vertex position along the longitudinal direction (z–axis). Fig.6.7 shows the distribution of the vertex position parameters. In particular, r_0 is assigned a sign depending on the sign of the y coordinate of the vertex. The resolutions on the vertex coordinate are lower than 1 mm: this represents an improvements with respect to the resolutions foreseen for the track reconstruction in the MEG Spectrometer ($2.1 \div 2.5$ mm). However, we remind that this a preliminary result coming out from a study performed on a track sample generated from a point like vertex, whereas in the experiment the mean decay vertexes will be spread out on the extended target.

6.4.3 The Parameter Resolution

The quality of the reconstructed particle parameters and the estimate of their errors from the reconstruction in a subdetector is essential for matching and propagation into another subsystem.

As seen in the previous section, the quality of a determination of a track parameter X_i is reflected into the parameter residual defined as

$$R(X_i) \quad = \quad X_i^{rec} - X_i^{true}$$

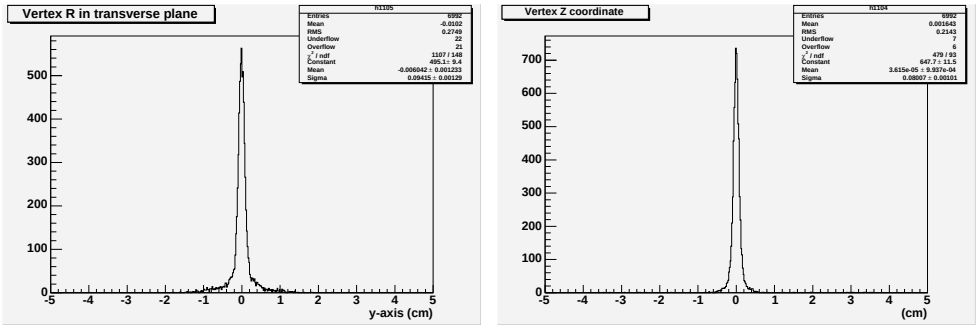

(a) (b)

Figure 6.4: *Vertex position after the fitting step both in the transverse (a) and in the longitudinal (b) planes.*

From its distribution, one can obtain the bias $\langle R(X_i)\rangle$ on the parameter estimate, and the resolution from the width $(\sigma(R(X_i)))$.

However, having calculated the parameter covariance matrix it is also possible to define the normalized residual

$$P(X_i) \quad = \quad \frac{X_i^{rec} - X_i^{true}}{\sqrt{C_{ii}}} \tag{6.12}$$

which is often called the pull of the parameter. Ideally, the pull should statistically follow a Gaussian distribution with a mean value of zero and a standard deviation of one.

Using (6.12) and the relations in (6.11) it is possible to define the normalized residual for the track parameters and their distributions are shown in fig.6.5. Although the distribution of the pulls for the angular variables are Gaussian, their width is larger than unity (1.2 and 1.7 for $\cos\theta$ and φ respectively). Moreover, even if the pull on the momentum has a distribution standard Gaussian–like (the $mean = -0.04$ and the $\sigma = 1.04$) it shows some non Gaussian tails. An explanation of these problems is an underestimate of the error matrix that seems to depend on

- wrong coordinates for some input hits (contributing to the tails);
- problem with Multiple Scattering and energy loss corrections to the covariance matrix (contributing to the φ and θ resolutions).

The first problem might arise from wrong left–right assignment in the calculation of the hit coordinates. As a matter of fact, a check on the hit position

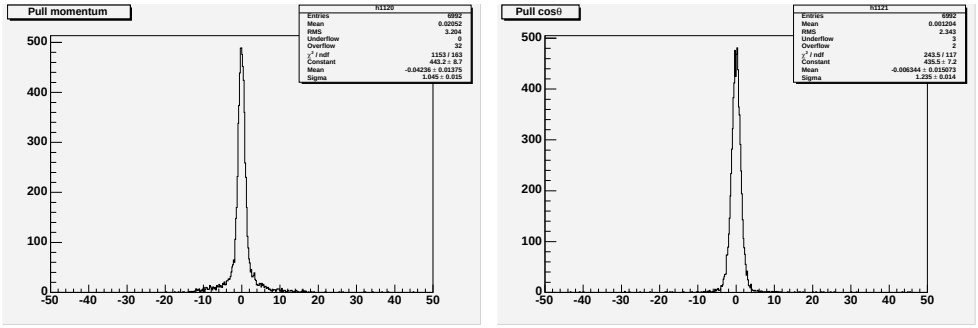

(a) (b)

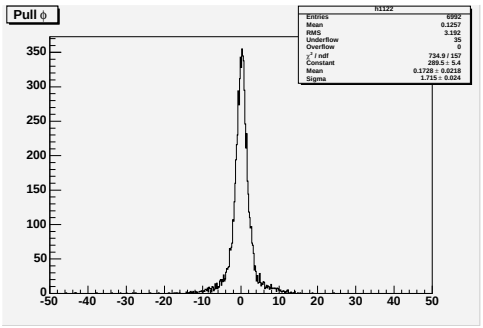

(c)

Figure 6.5: *Normalized parameters distributions for momentum (a),* $\cos\theta$ *(b) and* φ *(c) respectively.*

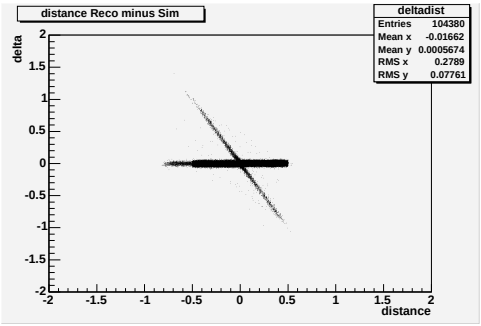

Figure 6.6: *Scatter plot for hit distance: on the y–axis is plotted the difference between the hit position after simulation and after reconstruction, on the x–axis the hit distance from the sense wire after the simulation is reported.*

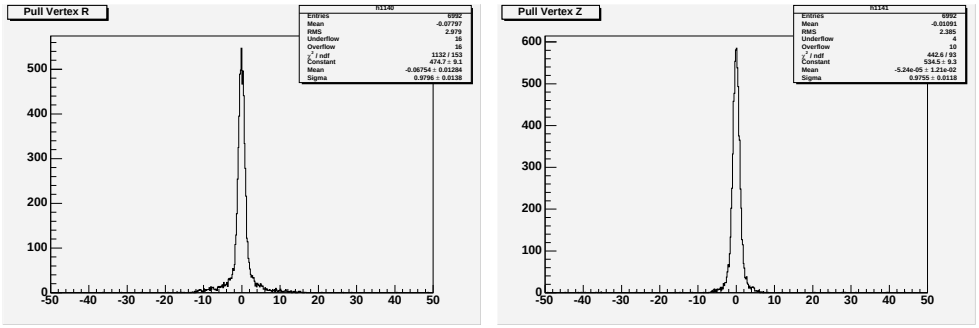

(a) (b)

Figure 6.7: *Pulls for the vertex position after the fitting step: (a) pull for r_0, (b) pull for z_0.*

after simulation and after the pattern recognition shows (see fig.6.6) as of about 3% of the reconstructed hits have a wrong assignment of the left–right side. The second could be due to a mismatch in the treatment of the Multiple Scattering and energy loss in simulation and in the fit.

Obviously, these problems affect the resolution on all parameters, including the track vertex coordinates. With reference to fig.6.7, where the pulls for r_0 and z_0 are shown, we notice again same non Gaussian tails.

From this preliminary study of the Kalman track fit performance in MEG, it is clear that the target accuracy can be achieved with the detector design chosen by the collaboration. Further refinements in the evaluation of the errors, which seems to be necessary in order to tune the pattern recognition and track fit algorithms performance, can be achieved with the standard procedures and in any case would be required again on real where, for example, misalignments and miscalibration of the detectors will introduce new uncertainties in the measurements.

Conclusions

In this work a review of the theoretical and experimental motivations for searching for LFV has been given. In particular the detection of the $\mu^+ \to e^+\gamma$ decay would be a very good opportunity for priming scenario down the physics beyond the SM, since many SUSY models predict a measurable ($\geq 10^{-14}$) branching ratio.

The MEG experiment at PSI Laboratory of Zurich (CH) is designed to search for LFV decay $\mu^+ \to e^+\gamma$ with a sensitivity of $\sim 5 \times 10^{-14}$ on *B.R.*, representing an improvement of about two order of magnitudes with respect to the present limit quoted in the PDG.

To have a successful results, the experiment must be ables to measure the photon and positron four momentum and the vertex decay with very high efficiency and precision.

My contribution to the experiment as a member of the Lecce group has been to develop a track finding algorithm for positron tracks in the spectrometer, which has been widely described in the Chapter 5, and perfectly integrated in the Offline System (MegRoot) developed by the Lecce group.

Starting from the raw data format, defined by the collaboration, the algorithm is able to cluster the hits belonging to the track in the time with the trigger (track segments) rejecting both hits from noise and those belonging to pile–up tracks. Moreover, the algorithm gives an estimate of the initial kinematic parameters of the track (momentum and flight direction) which are shown to be useful for the final fitting step.

The track finding performances are within the specifications. A study performed with two different samples of positron events (the first one with only the positron from Michel decay has been used, while in the second one also the positron from $\mu \to e\gamma$ decay are used) gives an algorithm efficiency to collect the hits belonging to the track correlated to the signal trigger greater of 94%; in particular it achieves $(99.2 \pm 0.1)\%$ when the track in

time with the trigger is due to the positron from the $\mu \to e\gamma$ decay. Again, for about 2/3 of the events, the track finding is able to reject the pile–up tracks clustering only the hit belonging to the trigger track. For each cluster of hits the kinematic track parameters are evaluated by a linear correlation from these and the geometric properties of the track (i.e. the bending radius and the track depth along the longitudinal direction) with resolutions which are shown to be adapt for a starting condition to track fit.

In the end, the event reconstruction chain has been completed by matching the track finding algorithm with the fit program: a track model based on the Kalman filter.

A preliminary study on the fitting procedure shows that it is possible to obtain the track parameters with a precision better of 0.9% in FWHM for the momentum and of about 3 *mrad* on the flight direction, in perfect agreement with the design resolution of the spectrometer.

Acknowledgments

I wish to thank all the people that have helped me during my doctoral course; in particular my advisor Dr. Stefania Spagnolo for the continuous support she gave me and for her guidance throughout the past three years. Moreover, I thank her for the meticulous work correction and, above all for her infinite patience with which she has tolerated my exponential increase of entropy.

I thank Prof. Franco Grancagnolo for his technical suggestions but also for the opportunity that he has given me to carry out my research activity inside to the I.N.F.N. Lecce group. Moreover, I thank the people of the MEG–Lecce group of which I have been a member: Corrado, Anna, Vito, Giusy, Giovanni, Emanuela and Sergio (that has lived with me the Siberian winter experience), with all of them I have shared a nice working experience.

Additional thanks go to Dr. Paolo Ciafaloni, from I.N.F.N Lecce, who driven me in the theoretical complex scenarios and to Dr. Fedor I. Ignatov, from Budker Institute of Nuclear Physics (BINP) of Novosibirsk (Rus), for his help on the Kalman filter development.

At the end my thanks go to my friends that have directly or indirectly contributed to complete this work:

Andrea Ventura, the expert of scripting language and leader group of the CdSR (a virtual association of the *Little Flowers* physicists);

Gianfranco, the misunderstood genius of the PCs and with whom I faced many work trips;

Karen for the profuse encouragement given me to solve **her** many software problems;

Alessandro and Marco the theoretical members of CdSR;

Michele, the connection point with the ATLAS Lecce group and chairman of nice parties at his sea–side house.

Special thanks go to beautiful and nice girls with whom I shared the office, Giovanna, Tina and Letizia. In particular to Giovanna and Tina who relevantly contributed to writing this book with their gossip and relax moments.

Moreover, my thanks go to all the people that are not mentioned here, but have supported and tolerated me in these years.

Bibliography

[1] Y. Fukuda *et al.*, *Super–Kamiokande Collaboration* hep–ex/9803006 and hep–ex/9805006.

[2] for reviews, see:
E.S. Abers and B.W. Lee, *Phys. Rev.* **9**(1973), 1;
M.A.B. Beg and A. Sirlin, *Phys. Rep.* **88**(1982), 1;
P. Langacker, *Phys. Rep.* **72**(1981), 185;
P. Langacker and J. Erler, *Phys. Rev.* **D50**(1994), 1304.

[3] H. Weyl, *Z. Phys.***56**(1929), 330;
C.N. Yang and R. Mills, *Phys. Rev***96**(1954), 191.

[4] R.D. Field, *Perturbative QCD* (Addison–Wesley, Redwood City, 1989);
F.J. Yndurain, *The Theory of Quark and Gluon Interactions* (Springer–Verlag, Belin, 1993).

[5] S.L. Glashow, *Nucl. Phys.* **22**(1961), 579;
S. Weinberg, *Phys. Rev. Lett.* **19**(1967), 1264.

[6] B.W. Lee, *Chyral Dynamics* (Gordon and Breach, NY, 1972);
S. Coleman, *Aspect of Symmetry* (Cambridge Univ. Press., Cambridge, 1985).

[7] L.J. Hall, V.A. Kostelecky and S. Raby: *Nucl. Phys.* **B267**(1986), 415.

[8] S. Dimopoulos and D. Sutter *Nucl. Phys.* **B452**(1995), 496.

[9] H. Georgi and S. Glashow, *Phys. Rev. Lett.* **32** (1974), 438.

[10] S. Dimopoulos, S. Raby and F. Wilczek, *Phys. Rev.* **D24**(1981), 1681.

[11] R. Barbieri, L.J. Hall, A. Strumia, *Nucl. Phys.* **B445**(1995), 219.

[12] M. Olechowski and S. Pokorski, *Phys. Lett.* **B257**(1991), 388.

[13] T. Yanagida, *Proceedings of Workshop on Unified Theory and Baryon Number in the Universe*, edited by O. Sawada and A. Sugamoto (1979). E.Kh. Akhmedov, G.C. Branco and M.N. Rebelo, *hep–ph/9911364*.

[14] Z. Maki, M. Nakagawa and S. Sakata, *Prog. Theor. Phys.* **28**(1962), 870.

[15] S.M. Bilenky and B. Pontecorvo, *Phys. Rep.* **41**(1978), 225–261.

[16] Ta–Pei Cheng and Ling–Fong Li, *Gauge theory of elementary particle Physics*, Oxford Science Publications (1984).

[17] G. Signorelli, Ph.D Thesis (2005).

[18] R. Barbieri, L.J. Hall, *Phys. Lett.* **B228**(1994), 212.

[19] P. Ciafaloni, A. Romanino and A. Strumia, *Nucl. Phys.* **B458**(1996), 3.

[20] J. Hisano *et al.*, *Phys. Lett.* **B357**(1995), 576
J. Hisano *et al.*, *Phys. Rev.* **D53**(1996), 2442
J. Hisano *et al.*, *Phys. Lett.* **B391**(1997), 341.

[21] C. Fronsdal and H. Überall, *Phys. Rev* **118**(1959), 654.

[22] S.G. Eckstein and R.H. Pratt, *Ann. Phys.* **8**(1959), 297.

[23] Particle Data Group (2004)
http://pdg.lbl.gov

[24] Y. Kuno and Y. Okada, *Phys. Rev. Lett.* **77**(1996), 434.

[25] L. Michel, *Proc. Phys. Soc.* **A63**(1950), 514.

[26] C. Bouchait and L. Michel, *Phys. Rev.* **106**(1957), 170.

[27] V.A. Boranov *et al.*, *Sov. J. Nucl. Phys.* **53**(1991), 852.

[28] C. Dohmen *et al.*, *Phys. Lett.* **B317**(1993), 631–636
W. Honecker *et al.*, *Phys. Rev. Lett.* **76**(1996), 200–203
J. Kaulard *et al.*, *Phys. Lett.* **B422**(1998), 334–338.

[29] V.W. Hughes *et al.*, *Phys. Rev. Lett.* **5**(1960), 63–65.

[30] G. Feinberg and S. Weinberg, *Phys. Rev. Lett.* **123**(1961), 1439.

[31] L. Willmann *et al.*, *Phys. Rev. Lett.* **82**(1999), 49.

[32] E.P. Hincks and B. Pontecorvo, *Phys. Rev. Lett.* **73**(1947), 246.

[33] S. Lokonathan and J. Steinberg, *Phys. Rev.* **98**(1955), 240.

[34] K. Nishijima, *Phys. Rev.* **108**(1957), 907
J. Schwinger, *Ann. Phys.* **2**(1957), 407.

[35] G. Danby *et al.*, *Phys. Rev. Lett.* **9**(1962), 36.

[36] MEGA Collaboration, M.L. Brooks *et al.*, *Phys. Rev. Lett* **83**(1999), 1521
MEGA Collaboration, M. Ahmed *et al.*, *Phys. Rev.* **D65**(2002), 112002.

[37] MEG Collaboration, *The MEG experiment: search for the* $\mu^+ \to e^+\gamma$ *decay at PSI*, Reaserch Proposal to INFN (September 2002).

[38] A. Badertscher & al., *PSI Users's Guide, Accelerator Facilities*, PSI internal report (1989).

[39] MEG Collaboration, *Beam Line Development for the MEG Experiment*, PSI Annaual Report, (2003).

[40] PSI Scientific Report 2002–2003, Volume I.

[41] T. Mori *et al.*, *Search for* $\mu^+ \to e^+\gamma$ *down to* 10^{-14} *branching ratio*, Proposal to PSI (1999).

[42] J. Allison *et al.*, *Nucl. Instr. and Meth.* **A310**(1991), 527.

[43] BELLE Collaboration, *BELLE Technical Design Report*, KEK Report 95–1(April 1995).

[44] BaBar Collaboration, *Technical Design Report*(March 1995).

[45] O. Nitoh *et al.*, *J. Appl. Phys.* **33**(1994), 5929.

[46] Muegamma Technical Note TN013 (http://meg.psi.ch/docs/index.html)

[47] MEG Collaboration, *MUEGAMMA timing counter prototype test*, PSI Annaual Report, (2001).

[48] F. Gatti, *Status of the MEG Timing Counter*, available at http://meg.psi.ch/docs (February 2004).

[49] A. Baldini *et al.*, *Liquid Xe scintillation calorimeter and Xe optical properties*,

[50] J. Hout and T.K. Bose, *J. Chem. Phys.* **95**(1991), 2683.
H.J. Achtermann, *J. Chem. Phys.* **98**(1993), 2308.
U. Hohm, *Molecular Physics* **81**(1994),157.

[51] MIDAS home page, http://midas.psi.ch

[52] http://root.cern.ch/root/

[53] http://aliweb.cern.ch/offline/

[54] *Detector Description and Simulation Tool*, Application Software Group CERN, CERN Program Library Writeup W5013 (1993)

[55] ALICE Collaboration, *The Virtual MonteCarlo*, proceedings of "Computing in High Energy and Nuclear Physics", 24–28 March 2003, La Jolla, California.

[56] D.H. Wilkinson, *Ionization Chambers and Counters*, Cambride University Press, Cambridge (1950).

[57] P. Billoir *et al.*, *Nucl. Instr. Meth* **A241**(1985), 115.

[58] G. Terracciano, *Reconstruction Class*, MEG software workshop, Lecce(Italy) June 21–22 2005.

[59] W. Blum and L. Rolandi, *Particle Detection with Drift Chamber*, editing by Springer–Verlag Berlin Heidelberg 1993

[60] ALICE Collaboration, *Production of Compressed and Uncompressed Raw Data for ALICE Data Challange.*

[61] C. Chiri *et al.*, *Pattern Recognition in the MEG Spectrometer*, MEG–TN027, September 19 (2005).

[62] R.E. Kalman, *A new approach to linear filtering and predictions problems*, Trans. ASME J. Basic Eng. **82**(1960), 35–45.

[63] W.T. Scott, *Rev. Mod. Phys.* **35**(1963), 231.

[64] V.L. Highland, *Nucl. Instrum. Methods* **149**(1975), 497 and **161**(1979), 171.

[65] *Phys. Rev.* **D50**(1994), 1253.